Fiber optic sensors for industry and military applications

Yiyang Zhuang

FIBER OPTIC SENSORS FOR INDUSTRY AND MILITARY APPLICATIONS

by

YIYANG ZHUANG

A DISSERTATION

Presented to the Graduate Faculty of the

MISSOURI UNIVERSITY OF SCIENCE AND TECHNOLOGY

In Partial Fulfillment of the Requirements for the Degree

DOCTOR OF PHILOSOPHY

in

ELECTRICAL ENGINEERING

2021

Approved by:

Dr. Jie Huang, Advisor
Dr. Steve Watkins
Dr. Rui Bo
Dr. Mina Esmaeelpour
Dr. Aditya Kumar

PUBLICATION DISSERTATION OPTION

This dissertation consists of the following three articles that have been published as follows:

Paper I, found on pages 7–27, has been published in *Optics Express*.

Paper II, found on pages 28–60, has been published in *IEEE Transactions on Instrumentation and Measurement*.

Paper III, found on pages 61–89, has been published in *Journal of Neuroscience Methods*.

ABSTRACT

Fiber optic sensors (FOSs) have been widely used for measuring various physical and chemical measurands owing to their unique advantages over traditional sensors such as small size, high resolution, distributed sensing capabilities, and immunity to electromagnetic interference. This dissertation focuses on the development of robust FOSs with ultrahigh sensitivity and their applications in industry and military areas.

Firstly, novel fiber-optic extrinsic Fabry-Perot interferometer (EFPI) inclinometers for one- and two-dimensional tilt measurements with 20 nrad resolution were demonstrated. Compared to in-line fiber optic inclinometers, an extrinsic sensing motif was used in our prototype inclinometer. The variations in tilt angle of the inclinometer was converted into the cavity length changes of the EFPI which can be accurately measured with high resolution. The developed fiber optic inclinometers showed high resolution and great temperature stability in both experiments and practical applications. Secondly, a smart helmet was developed with a single embedded fiber Bragg grating (FBG) sensor for real-time sensing of blunt-force impact events to helmets. The combination of the transient impact data from FBG and the analyses using machine-learning model provides accurate predictions of the magnitudes, the directions and the types of the impact events. The use of the developed smart helmet system can serve as an early-stage intervention strategy for mitigating and managing traumatic brain injuries within the Golden Hour.

ACKNOWLEDGMENTS

First of all, I would like to express my sincere gratitude to my advisor Dr. Jie Huang. It is my great honour to work with him in Lightwave Technology Lab. I thank him for his continuous support, invaluable advice and patient guidance during my Ph.D. study. And I thank him for providing me opportunities to involve in all kinds of projects, which developed not only my skills as a researcher and engineer, but also the abilities to collaborate and communicate with others.

I am grateful to Dr. Steve Watkins, Dr. Rui Bo, Dr. Mina Esmaeelpour and Dr. Aditya Kumar for being my committee members. I want to thank them for their great advices for my research in these years.

Also, I would like to express my appreciation to Dr. Rex Gerald and Dr. Qingbo Yang for their consistent supports and beneficial discussions in my projects. It is my pleasure to collaborate with such excellent researchers in my Ph.D study.

I owe a special deal of gratitude to my collaborators of the projects, Taihao Han and Ryan O'Malley. I also would like to thank all of our lab members for their helps and discussions. And I appreciate the sponsors of the project, especially Leonard Wood Institute, Army Research Laboratory and Los Alamos National Lab.

Finally, I would like to thank my family members for their continuous support, especially my wife Lili Zheng who sacrifices a lot for me and our dear daughter Yunqi Zhuang.

TABLE OF CONTENTS

LIST OF ILLUSTRATIONS

1. INTRODUCTION

1.1. BACKGROUND

A fiber optic sensor (FOS) is a sensor that either utilize optical fiber as a sensing element or communication path of the signal from an external sensing head [1, 2]. Comparing with traditional electric sensors, FOS provides a promising solution for various applications owing to its unique advantages such as light weight, compact size, low cost, low transmission losses, electromagnetic interference immunity, capability for multiplexing and distributed sensing, etc. [3]. In recent years, FOSs have attracted increased attentions from researchers and numerous FOSs have been studied, designed, developed and even commercialized for appications in different areas including structural health monitoring [4-7], aerospace [8-12], military [13, 14], industry [15-17], etc..

Among all the developed FOSs, fiber Bragg gratings (FBGs) have attracted many interest in various sensing applications such as strain [18-21], temperature [22-24], vibration [25-27], etc.. An FBG is formed by creating a periodic refractive index variation along with the core of an optical fiber. The periodic pattern along the core can function as a notch filter that reflects the light with a particular wavelength and transmit others [28]. In comparison with other FOSs, FBG is suitable for mass-production due to its fabrication method. Meanwhile, the demodulation method of the FBG signals is relatively simple and fast (e.g., tens of kHz), which is capable of dynamic sensing scenarios like acoustic sensing or impact wave sensing. In addition, it is feasible to cascade multiple FBGs (typically up to several hundred) in one piece of optical fiber without influencing their sensing functionalities, which significantly decreases the installation complexities of the sensor array. The aforementioned features lead to the result that FBG is currently one of the most widely used and most successfully commercialized FOS.

Meanwhile, fiber optic interferometric sensor is also a promising candidate in various sensing applications [29-37]. The sensing principle of the fiber optic interferometric sensor is based on the demodulation of the interference pattern generated by two or multiple lights. The features of the interference pattern such as frequency, phase and amplitude can be used to calculate the optical path difference variation of the interferometer introduced by desired measurands like temperature, strain, etc. Nowadays, fiber optic interferometric sensors consist of four typical structures: Fabry-Perot (F-P), Michelson, Mach-Zehnder (M-Z), and Sagnac [38]. With the advantages of simple structure, small size, and easy in-line fabrication, a variety of fiber optic Fabry-Perot interferometer (FPI) sensors have been developed for measuring various parameters such as strain [39-42]and displacement [43, 44]. An FPI is usually formed by two parallel-arranged relectors. In the FPI sensor, the injected light along the fiber is partially reflected by two reflectors, respectively. And the interference pattern is generated by the lights reflected by two reflectors. For better signal-to-noise (SNR), the two reflectors of FPI are typically separated by 1 mm. Based on the cavity, the FPI sensors can be divided into two categories: intrinsic FPI (IFPI) sensors and extrinsic FPI (EFPI) sensors. For an EFPI sensor, a cleaved end of the optical fiber usually serves as one reflector, while the other reflector of EFPI can be a flat surface made by different materials such as metal and glass. Thus, the FPI is formed outside of the optical fiber. On the other hand, in an IFPI sensor, the two parallel reflectors are inscribed inside the core of the optical fiber. Therefore, the FPI cavity is inside the optical fiber. These two types have their respective advantages and disadvantages in practical applications. For the EFPI sensor, since the cavity of FPI is not limited inside the optical fiber, the structure design of the sensor is more flexible. In addition, the optical property of the cavity can be easily modified to fulfill the specific sensing application, especially in refractive index (RI)-related chemical or gas sensing. But the alignment of two reflectors with high precision during sensor fabrication is required, which increases the complexity of sensor fabrication. Meanwhile, it is hard to cascade multiple EFPI sensors on a single optical fiber. On the other hand, a series of IFPI sensors can be cascaded on an optical fiber, which is feasible for quasi-distributed sensing. But high-cost equipment such as femtosecond laser [45] or chemicals for etching [46] is required for reflector fabrication. The low-reflectivity reflector of the IFPI sensor is a factor that may influence its SNR in sensing application.

1.2. MOTIVATION IN THE DEVELOPMENT OF FIBER OPTIC SENSORS

Over the past decades, it is doubtless that the progress in the development of FOSs has greatly expanded their application scopes in the industry and military. However, there still remains several challenges in the development of FOS.

Firstly, despite the aforementioned advantages of FOSs over traditional sensors, the optical fiber itself is still fragile. Thus, for the applications in the the military and industry, the packaging of FOS is significant. The function of the packaging is not only to protect the FOS from the harsh environment, but also to minimize the debonding between FOS and its corresponding transducer. For example, in the sensing applications with FBGs, normally the deployed FBG is attached to the transducer with adhesives like epoxy. This may have longevity issues such as the debonding between FBG and the transducer.

Meanwhile, the transfer of the measurands between the transducer and FOS can vary with different packaging methods, which requires extra calibration to the FOS. An alternate method to avoid these issues is to develop extrinsic FOSs. Since in extrinsic FOSs the optical fiber only acts as the relay of the optical signal, commercialized optical fiber cable can be used in sensor fabrication, which is much more robust than bare optical fiber. With the proper structure design, the robustness of the FOS can be significantly enhanced while the essential functions and properties of the FOS, such as remote sensing capabilities and high resolution, remain.

Secondly, a FOS system with ultra-high sensitivity, high resolution, fast response time, and high-signal to-noise ratio produces raw data that is exceedingly rich in information, including signals corresponding to apparent “noises” [47]. The hidden correlation between the measurands and the sophisticated phenomenon might be revealed from these “noises”, which could greatly expand the application scopes of FOS. However, it is extremely hard to figure out the correlation with traditional data analysis methods such as modeling-based finite element analysis. Plus, traditional data analysis methods only aim to a specific case, which is inefficient to serve as a general approach in the application of FOS. The aforementioned factors limit the broadening of the sensing capabilities of the FOS. To overcome this limitation, very recently, machine-learning (ML) method is introduced as a combination with FOSs to enhance analytical capabilities for the complex transient signals [28]. As one of the most rapidly growing technical fields, the development of ML has dramatically influenced both science and industry areas since ML provides a novel and efficient way to analyze the high-throughput data and the desired input-outpout behavior [27, 48-51]. The ML models befits for FOS signal analysis because such models trained rigorously by a high-quality database are able to not only indicate the hidden linkage between sensor signal and monitored properties but also predict those properties in new signal data-domains.

1.3. CURRENT ACHIEVEMENT AND FUTURE WORK

Recently, we have proposed a novel optical fiber extrinsic Fabry-Perot interferometer (EFPI) for tilt measurements with 20 nrad resolution [52]. Compared to in-line fiber optic inclinometers, an extrinsic sensing motif was used in our prototype inclinometer. With a special design, the variation in the tilt angle of the inclinometer was converted into the cavity length change of EFPI, which can be accurately measured with high resolution. An EFPI-based two-dimensional (2-D) inclinometer with a similar structure was also demonstrated [53]. The designed EFPI-based inclinometers showed a high resolution, great temperature stability and excellent practicability in long-term test. In addition, we also developed a series of EFPI-based FOSs for different sensing applications such as strain, displacement, and pressure [40, 43, 44, 54].

Moreover, we exploited the combination of FOSs with ML to enhance our analytical capabilities for multifaceted analyses of complex transient signals. A smart helmet was developed with a single embedded fiber Bragg grating (FBG) sensor for real-time sensing of blunt-force impact events to helmets [28]. The combination of the transient impact data from FBG and the analyses using the machine-learning model provides accurate predictions of the magnitudes, the directions, and the types of the impact events. The use of the developed smart helmet system can serve as an early-stage intervention strategy for mitigating and managing traumatic brain injuries within the Golden Hour.

In the future, with the information-riched signals provided by the novel fiber optic inclinometers and the combination of ML models, we will continuously explore new capabilities for the devices we developed. We anticipate that in the near future, it will be possible to sense the movements of large objects such as submarines and trucks due to the modulation of gravity. We are looking forward that our work will inspire researchers with new possibilities of the sensing system design and it will have a significant impact on the sensing field.

PAPER

I. PROBING CHANGES IN TILT ANGLE WITH 20 NANORADIAN RESOLUTION USING AN EXTRINSIC FABRY-PEROT INTERFEROMETER-BASED OPTICAL FIBER INCLINOMETER

YIYANG ZHUANG,[1,3] YIZHENG CHEN,[1,3] CHEN ZHU,[1] REX E. GERALD II,[2] JIE HUANG,[1,*]

[1] Department of Electrical and Computer Engineering, Missouri University of Science and Technology, Rolla, MO 65409
[2] American Inventor Institute, Willow Spring, IL 60480, USA
[3] These authors contributed equally to this work.
*jieh@mst.edu

ABSTRACT

In this paper, we introduce and demonstrate a novel optical fiber extrinsic Fabry-Perot interferometer (EFPI) for tilt measurements with 20 nrad resolution. Compared with in-line optical fiber inclinometers, an extrinsic sensing structure is used in the inclinometers reported herein. Our design greatly improves on the tilt angle resolution, the temperature stability, and the mechanical robustness of inclinometers with advanced designs. An EFPI cavity, which is formed between endfaces of a suspended rectangular mass block and a fixed optical fiber, is packaged inside a rectangular container box with an oscillation dampening mechanism. Importantly, the two reflectors of the EFPI sensor remain parallel while the cavity length of the EFPI sensor meters a change in tilt. According to the Fabry-Perot principle, the change in the cavity length can be determined, and the tilt angle of the inclinometer can be calculated. The sensor design and the measurement principle are discussed. An experiment based on measuring the tilt angle of a simply supported beam induced by a small load is presented to verify the resolution of our prototype inclinometer.

The experimental results demonstrate significantly higher resolution (ca. 20 nrad) compared to commercial devices. The temperature cross-talk of the inclinometer was also investigated in a separate experiment and found to be 0.0041 μrad /°C. Our inclinometer was also employed for monitoring the daily periodic variations in the tilt angle of a windowsill in a cement building caused by local temperature changes during a five-day period. The multi-day study demonstrated excellent stability and practicability for the novel device. The significant inclinometer improvements in differential tilt angle resolution, temperature compensation, and mechanical robustness also provide unique opportunities for investigating spatial-temporal modulations of gravitational fields.

Keywords: Fabry-Perot, Fiber Optic Sensors, Gravity

1. INTRODUCTION

The inclinometers purposed for tilt measurements have attracted considerable attention for structural health monitoring and warning of impending natural disasters such as landslides and earthquakes [1-3]. The concept behind a typical inclinometer is that it measures variations in tilt angle generated by the behavior of a pendulum subject to a gravitational field [4].

For applications in harsh environments, modern inclinometers require high resolution and long measurement times to precisely and continuously measure variations in the tilt angle. Advanced applications require that inclinometers function in remote and unreachable places, requiring capabilities such as long distance transmission without loss and interference from electromagnetic sources, resistance to hazardous environments, etc.

[5]. The conventional electrolytic inclinometers, which have been widely used in practical applications, suffer from large transmission loss and electromagnetic interferences. However, fiber optic sensors could be promising candidates for inclinometers owing to their unique advantages such as immunity to electromagnetic fields, low transmission losses, high accuracy, the possibility of remote operation, robustness, etc. [6]. In recent years, a variety of fiber optic inclinometers have been reported and developed [7-16]. The majority of the previously reported fiber optic inclinometers are fabricated in-line (i.e., the sensor is fabricated using a piece of optical fiber), and the principles of sensing are based on wavelength or intensity modulation of the input signal caused by bending the fiber optic sensors as demonstrated for fiber tapers [7-11], fiber Bragg gratings (FBG) [12-14] and photonic crystal fibers [15, 16].

Although the inclinometers mentioned above show great capability in tilt measurement, there exist several drawbacks. For fiber taper-based fiber optic inclinometers, using a fiber taper can greatly reduce the mechanical strength of the sensor structure, which is too delicate for harsh environment. For FBG-based fiber optic inclinometers, one or more FBGs will be attached to a vertical cantilever-based pendulum and used to measure the strain variations of the cantilever caused by gravity-induced bending [12-14]. However, FBG-based inclinometers suffer from unwanted mechanical frictions, rotations, and instabilities because the force transfer from the cantilever to the FBGs is complicated. Furthermore, the accuracy of the FBG-based inclinometers will diminish in a vibrationally-unstable environment because the cantilever will experience a mechanical resonance [14]. Also, the resolution for all the aforementioned fiber optic inclinometers is less than 0.001° (17.5 μrad) [7-16], which is not sufficient for some applications like gravitational field measurement, which requires an extremely high precision tilt measurement [17].

Compared to the in-line structure fiber optic sensors, the extrinsic optical fiber sensors can overcome the disadvantage of low mechanical strength because the optical fiber only served as a transceiver of light signals. Recently, Lee et al. reported a packaged fiber optic inclinometer using a moveable transmissive grating panel, reflective mirror, and optical fibers as transceivers [5]. Their reported inclinometer achieved a full-scale measurement range from -90° to 90°. But the fabrication process for the transmissive grating panel is complicated. Meanwhile, a widely used interferometric sensor, the extrinsic Fabry-Perot interferometer (EFPI), has the merit for displacement and strain measurements [18-24]. An EFPI is formed by the endface of an optical fiber and an external reflecting surface. The cavity length of the EFPI (i.e., the distance between the two reflecting surfaces) can be accurately measured from the reflection spectrum [18]. Therefore, with proper structure design and packaging, an inclinometer based on EFPI displacement measurements will be able to take advantage of high resolution and could be considered as a good candidate for tilt measurements.

In this paper, we report a high resolution EFPI-based optical fiber inclinometer for tilt measurements. The reported inclinometer consists of an EFPI sensor packaged inside a rectangular metal container box. The sensor design and the measurement principles are discussed in Section 2. An example application experiment based on measuring the tilt angle of a cantilever, induced by small incremental loads (2.000g), is presented in Section 3 to verify the resolution of the novel inclinometer. Our results demonstrate high resolution

16.7 nrad. The novel inclinometer was also employed throughout five days to monitor the variations in the tilt angle of a windowsill caused by daily (cyclic) temperature changes.

2. SENSOR DESIGN AND MEASUREMENT PRINCIPLES

A schematic diagram of a partial side view of the inclinometer is illustrated in Figure 1(a). The EFPI sensor is fabricated and packaged in a rectangular metal container box. The EFPI sensor consists of two parts: the mass block part and the optical fiber module. The rectangular mass block is flexibly connected to the top plate of the rectangular container box by two stainless steel strand ropes of the same length. The distance between two connection points on the mass block and the corresponding connection points on the top plate are identical. The four connection points are contained in a common plane, and the stainless steel strand ropes are perpendicular to the horizontal plane of the inclinometer. As for the optical fiber module, a segment of the optical fiber is rigidly connected to the top plate of the rectangular box by a supporting rod. The supporting rod is perpendicular to the top plate, and the endface of the optical fiber is precisely adjusted to be parallel with the adjacent end face of the mass block. Therefore, the endface of the optical fiber and the adjacent endface of the mass block form an EFPI sensor. A thin layer of gold was sputtered onto the endface of the mass block to increase the reflectivity. When the inclinometer is tilted at an angle θ the two supporting ropes will remain perpendicular to the virtual horizontal Earth's ground plane as required by the Earth's gravitational field. Synchronously, the supporting rod will be tilted with the inclinometer, and the angle between the supporting rod and the ropes is the tilt angle of the inclinometer as illustrated in Figure 1(b). The mass block will remain parallel to the top plate because the four connection points define a parallelogram. As a result, the two reflectors of the EFPI sensor will remain parallel, but the distance between the two reflector surfaces will change. The change in the tilt angle of the inclinometer can be described as follow:

$$\Delta\theta = \arcsin\left(\frac{\Delta d}{l}\right) \tag{1}$$

where Δd is the change in the cavity length of the EFPI sensor and l specifies the lengths of the ropes. When the change in the tilt angle is small, Eq. (1) can be described as:

$$\Delta\theta = \arcsin\left(\frac{\Delta d}{l}\right) \approx \frac{\Delta d}{l} \tag{2}$$

Equation (2) shows that when the change in the tilt angle is small, the sensitivity of the inclinometer, which is defined as the ratio between the change in the cavity length and the corresponding change in the tilt angle (unit: nm/nrad), is uniquely determined by the rope length. Figure 1(c) is a partial schematic diagram of the inclinometer equipped with an oscillation dampening device. A cross paddle is connected to the bottom of the mass block, and it is immersed in a damping fluid. This arrangement can physically reduce oscillations from environment-induced vibrations and thereby increase the stability of the inclinometer. The oscillation reduction can also be achieved by a magnetic dampening device. A photograph of one prototype of the inclinometer is illustrated in Figure 1(d). To reduce the temperature cross-sensitivity of the inclinometer, during the fabrication of our inclinometer, the container box was initially backflushed with helium gas and then evacuated. Furthermore, all of the rigid components of the inclinometer, including the mass block, the supporting rod, and the rectangular box package, are made of Invar whose coefficient of thermal expansion, α_{CTE1}, is low (1.2×10^{-6}/°C). As revealed in Figure 1(a), when the temperature of the environment fluctuates, thermal expansions/contractions will affect the size of the mass block, the container box and the ropes; these size changes will

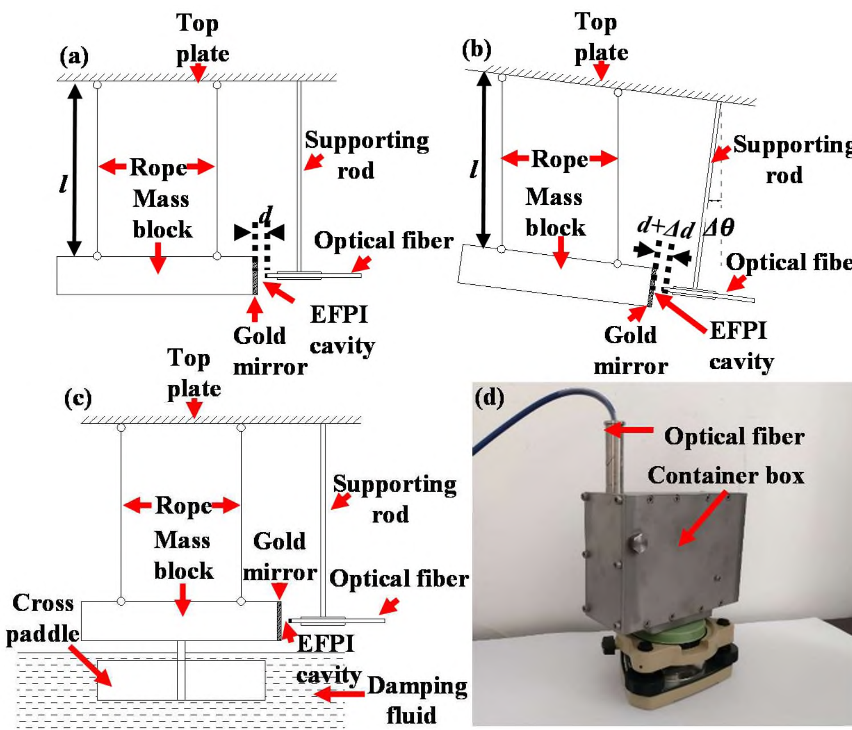

Figure 1. (a) Partial schematic diagram of the inclinometer. A rectangular mass block is flexibly connected to the top plate of the rectangular metal container box by two ropes with the same length. An optical fiber is rigidly connected to the top plate of the container box using a supporting rod. The EFPI sensor is formed by the combined endface of the optical fiber and the adjacent endface of the mass block. The endface of the mass block is sputtered with gold to form a highly reflective mirror surface. (b) Partial schematic diagram of the inclinometer tilted to an angle θ. The two endface reflectors of the EFPI sensor always maintain a mutual parallel disposition. (c) Partial schematic diagram of the inclinometer including an oscillation dampening device. The mass block is connected to a cross paddle which is immersed into a damping fluid. (d) Photograph of a prototype inclinometer. The inclinometer is made of Invar to reduce the temperature cross-sensitivity.

cause variations of the EFPI cavity length. The three effects result in a temperature cross-talk for the cavity length measurement. However, the contributing effects from mass block and container box will partially or completely offset each other. The result of geometrical considerations and analyses indicate that the change in the EFPI cavity length caused by a change in temperature can be described as:

$$\Delta d_t = \left(d\alpha_{CTE1} + l\theta\alpha_{CTE2}\right)\Delta T \tag{3}$$

where d is the initial cavity length of the EFPI; ΔT is the temperature change experienced by the inclinometer; θ is the tilt angle of the inclinometer to the perpendicular line and α_{CTE2} is the coefficient of thermal expansion of stainless steel.

As mentioned above, the endface of the optical fiber together with the adjacent reflective endface of the mass block form the EFPI sensor with a cavity length of d. The interference signal (I_0) is given by

$$I_0 = I_1 + I_2 + 2\sqrt{I_1 I_2}\cos\left(\frac{4\pi nd}{\lambda} + \varphi\right) \tag{4}$$

where I_1 and I_2 are the light intensities reflected from the endface of the optical fiber and the adjacent gold-sputtered mirror endface of the mass block, respectively; φ is the initial phase difference between the light waves reflected from the two reflectors; n is the refractive index of the cavity which is about 1 and λ is the wavelength of the incident light. When the variables inside the cosine function of Eq. (4) are equal to a multiple of 2π, a constructive interference results. In the wavelength spectrum of the interference signal, the space between two adjacent peaks, defined as the free spectrum range (FSR), can be expressed as:

$$FSR = \frac{\lambda_c^{\,2}}{2d} \tag{5}$$

where λ_c is the center wavelength of the interference spectrum. So, the cavity length can be demodulated by determining the FSR of the interference spectrum. When the inclinometer is tilted, the cavity length of the EFPI will experience a change. The change in cavity length can be evaluated by:

$$\Delta d = \frac{\lambda_c^{\ 2} \Delta FSR}{2 FSR_0 FSR_1} \tag{6}$$

where FSR_0 and FSR_1 are the values of FSR before and after the tilt, respectively; and, ΔFSR is the difference between FSR_0 and FSR_1. If the mass block module tilts clockwise, the cavity length of the EFPI will decrease. And, if the mass block module tilts counterclockwise, the cavity length of the EFPI will increase. Hence, the sign of ΔFSR can be used to determine the direction of tilt.

Concerning the demodulation principle shown above, variations of the cavity length of the EFPI can be determined. It should be noted that no matter how great the tilt angle is, the endface of the optical fiber will always be parallel to the adjacent reflective endface of the mass block. So, the tilt angle can be measured if the cavity length change is within a proper range (i.e., the cavity length of the EFPI is within 0 to 1 mm). More significantly, the measurement range and sensitivity of the inclinometer can be adjusted by simply changing the lengths of the stainless steel strand ropes, and adjusting the initial cavity length of the EFPI during the fabrication of the inclinometer. For example, if the lengths of the stainless steel strand ropes are 1.000 cm and the initial cavity length of the EFPI is 500.000 μm, the measurement range and sensitivity of the inclinometer are calculated to be -50 mrad to 50 mrad and 0.01 nm/nrad (cavity length change/tilt angle change), respectively. This adjustability feature expands the capability of our inclinometer for different tilt measurement applications.

3. EXPERIMENTAL RESULTS AND DISCUSSIONS

To verify the resolution of the prototype inclinometer, a calibration experiment based on measuring the tilt angle of a simply-supported beam under external load was designed and tested. The schematic diagram of the test experiment setup is illustrated in Figure 2(a). The beam is made of stainless steel. The size of the beam is 700.0 mm×50.0 mm×8.0 mm. The distance between each support point and the respective end of the beam is 100.0 mm, so the effective length of the beam is 500.0 mm. The inclinometer is placed at the same position as one of the support points. Several copper washers were placed on the center of the beam to provide the necessary load to cause the beam to bend and, therefore, tilt the beam at both support points. To prevent the copper plates from sliding, a node was soldered to the center of the beam, and each copper plate was fabricated with a small hole so they could be fixed on the node.

At the support points, the tilt angle can be expressed as:

$$\theta = \frac{Fl_s^2}{16EI} \tag{7}$$

where F is the load applied to the center of the beam; l_s is the length between the two support points; E is Young's modulus for the stainless steel beam material used in the experiment (about 200 GPa), and I is the moment of inertia. The test measurement setup for the inclinometer apparatus is illustrated in Figure 2(b). A wavelength interrogator (Micron Optics SM125) which integrates a swept laser, a photodetector, and an optical

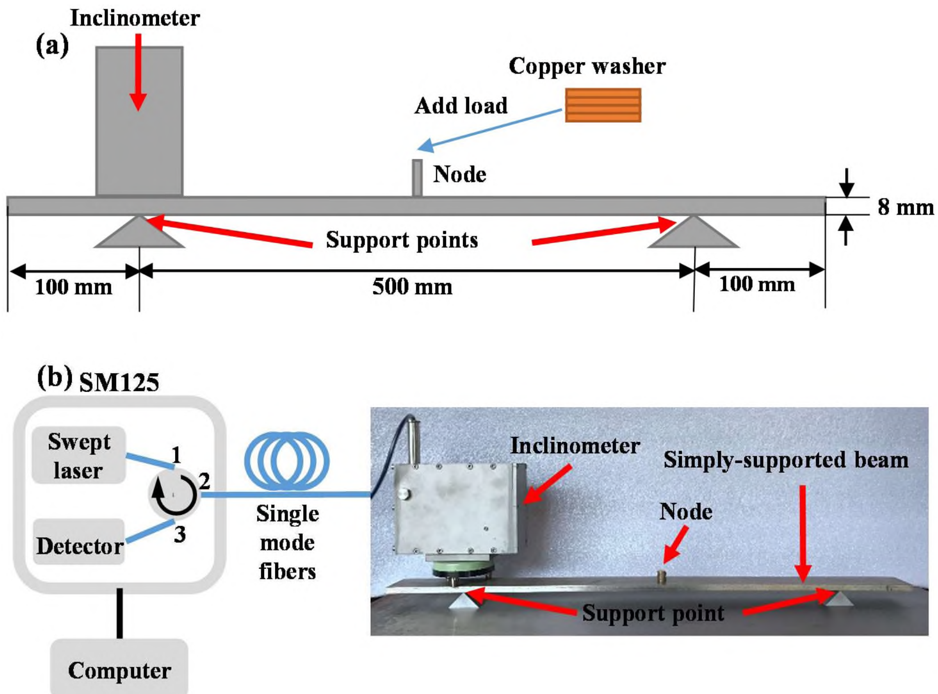

Figure 2. (a) Schematic cross-section diagram of the tilt angle calibration experiment based on a simply-supported beam. The inclinometer is placed at the location of a support point. Copper plates were used to provide the load for tilting the beam. (b) A photograph of the experimental test setup and the measurement equipment. Schematic diagram of the test measurement setup for the inclinometer. A Micron Optics SM125 was used as the source and demodulation device. A personal computer was used to analyze the interference spectra.

fiber coupler was used as the source and demodulation device. The incident light was directed into the inclinometer then reflected back to the interrogator through the single-mode fiber. The reflected spectrum was obtained by sweeping the wavelength of the laser (from 1510 nm to 1590 nm) and recording the corresponding intensities of the reflected signals. A personal computer was connected to the SM125 to record and analyze the interference spectra using a LabVIEW program developed in our lab. Detailed descriptions of the measurement apparatus can be found in our recent work [21-24].

Figure 3(a) shows the interference spectrum of the EFPI based inclinometer without a load applied to the beam. The averaged FSR of the spectrum is 5.071 nm, corresponding to the initial cavity length of 236.871 μm. In our calibration experiment, the cavity length was measured for 55 minutes. During the experiment, a copper plate was placed on the node of the beam every five minutes, and every minute the interference spectrum was recorded. Hence, for each load, five interference spectra were recorded to calculate the cavity length of the EFPI sensor. The weight of each copper plate is 2.000 g. The lengths of the ropes were set to 6.000 cm in the prototype inclinometer and the dynamic range of the inclinometer was calculated to be -8.333 mrad to 8.333 mrad. The silicone fluid with 500000 cSt was used as the damper fluid. The size for each paddle is 33 mm×11 mm×1 mm in the prototype inclinometer. According to Eq. (6), when a copper plate was placed on the center of the beam, it would induce a tilt angle of magnitude 0.717 μrad to the beam at each support point. The total load ranged from 0 to 20.000 g, corresponding to a tilt angle range from 0 to 7.170 μrad. The calibration results for the inclinometer are shown in Figure 3(b). The left vertical axis represents the measured cavity length of the EFPI sensor, and the right vertical axis represents the measured tilt angle, which was calculated from Eq. (2). In Figure 3(b), 0.717 μrad steps increments of the tilt angle can be easily distinguished. The measurement setup based on the SM125 can achieve a resolution of 1.0 nm for the cavity length. Thus, the EFPI based inclinometer can achieve a measurement resolution of 16.7 nrad according to Eq. (2). Multiple measurements of the cavity length and the corresponding tilt angle recorded when the applied load was 16.000 g are presented as an inset in Figure 3(b). We calculated that the standard deviation of the tilt angle measurement

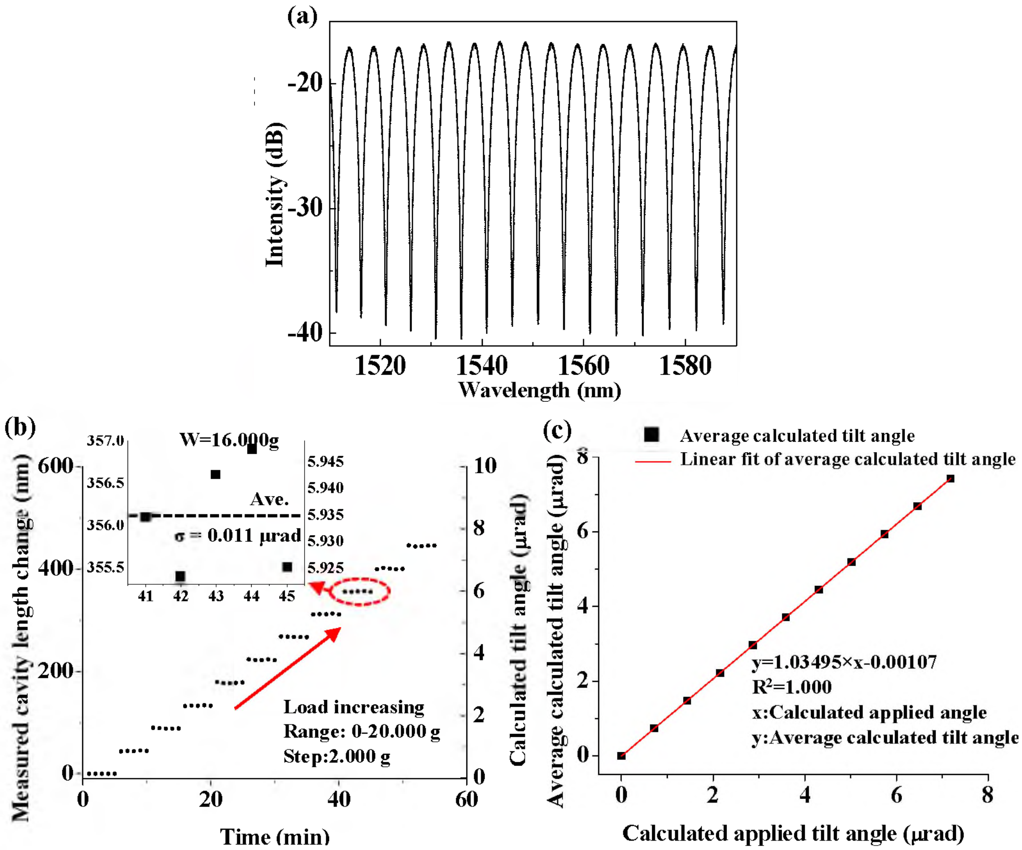

Figure 3. (a) Interference spectrum of the EFPI-based inclinometer without a load applied to the beam. The spectrum was recorded from 1510 nm to 1590 nm. (b)The calibration result of the EFPI-based inclinometer. The measured change in the cavity length and the calculated tilt angle are shown as a function of time. Every five minutes, the load was increased by 2.000 g, and every minute the interference spectrum was recorded. The inset shows the change in the cavity length and the measured tilt angle from 41 to 45 minutes. (c) The average calculated tilt angle correlated to the calculated applied tilt angle and a linear fit was the result. The equation for the linear fit is y=1.03495×x-0.00107, where y represents average calculated tilt angle and x represents calculated applied tilt angle.

uncertainty is 11.2 nrad. The measured variations are due to environmental perturbations such as temperature fluctuations, experimental setup vibration, etc. The measured tilt angle as a function of applied theoretical tilt angle is shown in Figure 3(c). The linear fit (red line) produced an R-square of 1.000, indicating an excellent correlation and linearity between the applied tilt angle and measured tilt angle. The slope and the intercept of the linear fit result reveal the difference between the applied tilt angle and measured tilt angle. The reason for the difference was that we use the angle calculated from Eq. (7) as the applied tilt angle, but the calculation was based on the assumptions that the tilt angle of our inclinometer was equal to the tilt angle of the beam at the support point, and the load was concentrated at the center of the beam. The error introduced by the mathematical approximation in Eq. (2) is much smaller than the deviation of the measured angle, which can be neglected.

The response of our prototype inclinometer to variations in temperature was investigated in a separate experiment. The experimental setup is illustrated in Figure 4(a). The inclinometer was placed inside a temperature-controlled box. Each side of the box was filled with insulating foam. A cylindrical fused silica base was used at the bottom of the box, and the prototype inclinometer was fixed on the top of the base because the fused silica has a more uniform thermal expansion effect than the insulation foam. Every hour, the temperature inside the box was increased by 10 °C. After 50 minutes of temperature stabilizing, the interference signal was recorded ten times in 10 minutes. The total temperature range is from 0-50 °C. The experimental results are demonstrated in Figure 4(b) and Figure 4(c).

Figure 4(b) illustrates the change in cavity length derived from all of the recorded interference signals recorded for the experiment and the corresponding equivalent tilt angles as a function of temperature. As shown in Figure 4(b) the change in the cavity length has a positive correlation with temperature. The standard deviation of the equivalent tilt

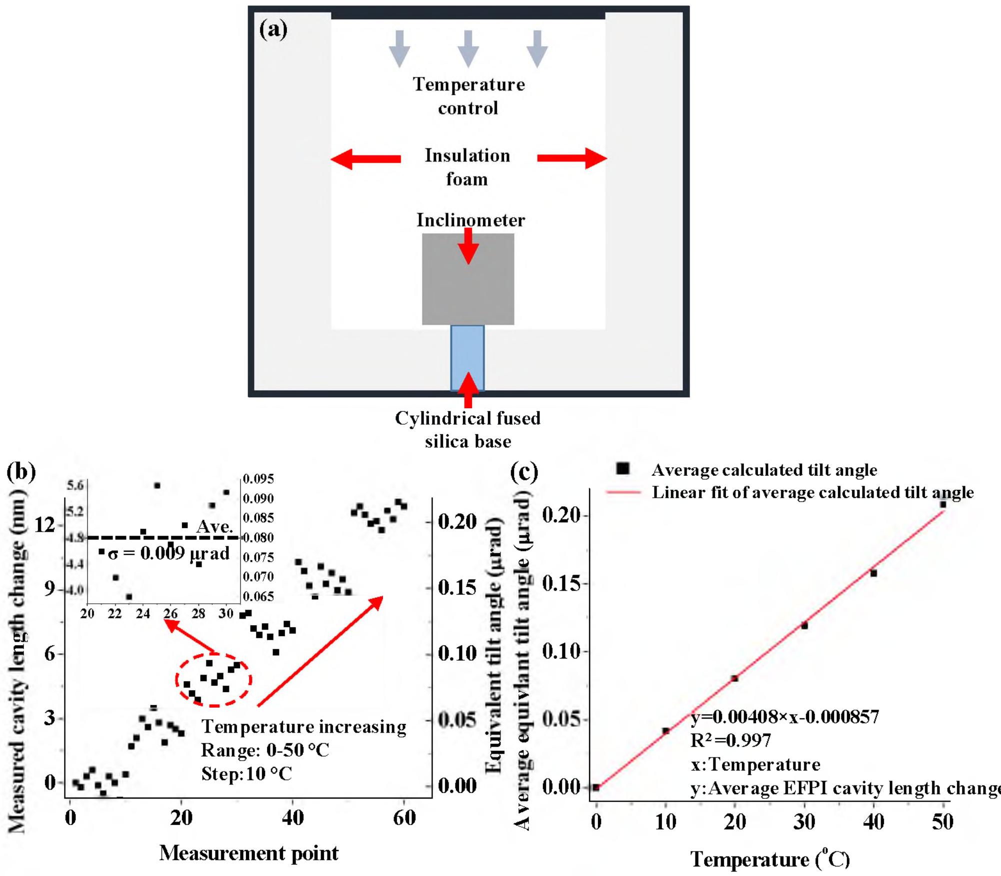

Figure 4. (a) Experimental setup for testing the response of the prototype inclinometer to variations in temperature. The inclinometer was placed inside a temperature-controlled box filling with insulating foam. The inclinometer was placed on a cylindrical fused silica base positioned at the bottom of the box. (b) EFPI cavity length change derived from all of the recorded interference signals as a function of temperature. The temperature in the temperature-controlled box was increased from 0 to 50 °C with a step size of 10 °C. (c) Average equivalent tilt angle change as a function of temperature. The linear fit result is shown as a red line. The slope of the linear fit result indicates that the temperature cross-talk for tilt angle measurements is 0.0041 μrad/°C.

angle at a constant temperature was about 9.3 nrad, which nearly matches the value presented in the inset of Figure 3(b). The average change in the cavity length as a function of temperature is illustrated in Figure 4(c). The slope of the linear fit result indicates that the temperature cross-talk for the cavity length measurement is 0.258 nm/°C, corresponding to a 0.0041 μrad /°C change in tilt angle according to Eq. (2). The measured temperature cross-talk result matches well with the theoretical result, which is calculated to be 0.279 nm/°C (or 0.0044 μrad/°C) according to Eq. (3) using the initial cavity length of 232.667 μm. The influence of the temperature cross-talk is small, and it can be limited by recording the temperature data for compensation or using a proper thermal insulation device. Furthermore, a combination of the inclinometer design and a judicious choice of structural materials for the top plate and the mass block (see Figure 1(a)) will reduce the temperature cross-talk to a negligible value. For example, a thin layer of metal with larger coefficient of thermal expansion than Invar, like copper, can be electroplated on the side of the mass block before gold sputtering process. In this way, the temperature cross-talk sensitivity of the inclinometer can be further reduced.

To verify the practicability of our prototype inclinometer, an experiment was conducted for monitoring variations in the tilt angle of a windowsill caused by periodic temperature changes. The experimental setup is illustrated in Figure 5(a). The inclinometer was placed on a marble windowsill inside a room, and it was sealed in a foam box, which kept the inside temperature constant and reduced the temperature influences on the inclinometer. The window is facing south. The interference signal of the EFPI sensor was recorded every ten minutes during a five-day period to calculate the tilt angle as a function of time (8:00 AM March 8th, 2017 – 8:00 AM March 13th, 2017).

Figure 5(b) shows the experimental results for monitoring variations in the tilt angle of the windowsill and the local temperature during five days versus the experiment time. The local area temperature data was obtained from [55]. As shown in Figure 5(b), the measured tilt angle and temperature curves map similar patterns, showing a strong correlation. Five peaks and five valleys can be observed in both plots presented in Figure 5(b). The

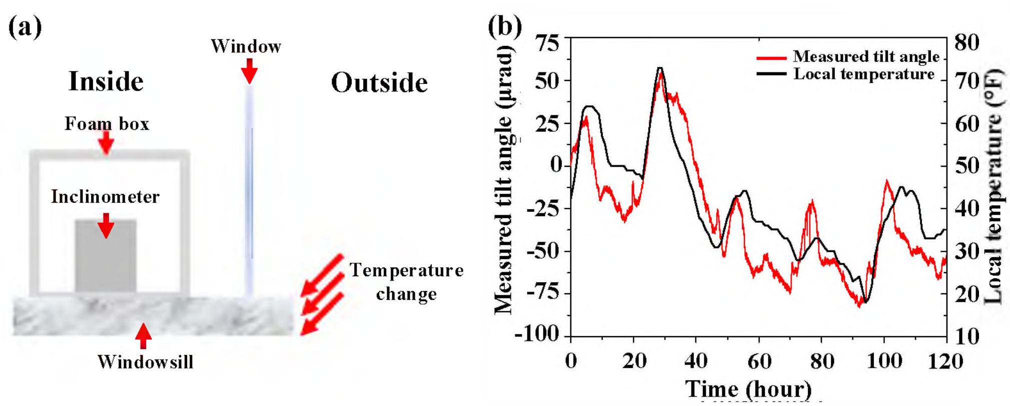

Figure 5. (a) The experimental setup for monitoring variations in the tilt angle of a windowsill caused by periodic changes in temperature. The inclinometer was placed on a marble windowsill, and it was sealed in a foam box, which kept the temperature inside constant and reduced the influence of temperature on the inclinometer. The window is facing south. (b) The measured tilt angle of a windowsill and local temperature change as a function of time during a five-day measurement period (from 8:00 AM on March 8th, 2017 to 8:00 AM on March 13th, 2017). An interference spectrum was recorded every ten minutes, and the cavity length was measured to calculate the tilt angle. The measured tilt angle and the published local area temperature curve follow a similar trend, showing that they are correlated. Five peaks and five valleys can be observed in both curves, corresponding approximately to 2 PM and 3 AM every day, respectively.

corresponding times for the peaks were similar, approximately 2 PM each day during the five days, while the corresponding times for the valleys occurred at approximately 3 AM each day during the five days. The results show that the tilt angles of the windowsill caused by temperature changes reached maxima in the afternoons. Interestingly, the passage of clouds during the day was also noticed by measurable changes in the tilt angle of the windowsill because the sunlight was blocked which resulted in small temperature changes of the building and concomitant deformation in the building structure. This experiment demonstrates that our inclinometer shows high resolution and excellent stability.

4. CONCLUSIONS

In this paper, we report and demonstrate an EFPI-based fiber optic inclinometer for tilt measurements with high-resolution capability, 20 nrad, a resolution that is much higher than the resolution capabilities reported for all of the previously published fiber optic inclinometers and commercially available inclinometers. Compared to in-line fiber optic inclinometers, the extrinsic sensing motif was used in our prototype inclinometer. Our inclinometer consists of an EFPI-based sensor packaged inside a rectangular container box. A rectangular mass block is flexibly connected to the top plate of the rectangular container box by two Stainless steel strand ropes of the same lengths. An optical fiber is rigidly connected to the top plate of the rectangular container box by a supporting rod. Therefore, the endface of the optical fiber and the adjacent mirror endface of the mass block serve as the two reflectors of an EFPI sensor. To reduce the effects of oscillations, the rectangular mass block is connected to a cross paddle, which is immersed in a damping fluid. After tilting, the two endface reflectors of the EFPI sensor will remain parallel while the cavity length of the EFPI sensor will experience a change. According to the Fabry-Perot principle, the change in the cavity length can be determined, and the tilt angle of the inclinometer can be calculated. The sensor design and the measurement principles are discussed. An experiment based on measuring the tilt angle of a simply-supported beam induced by a small load is presented to verify the resolution of the prototype inclinometer, demonstrating high resolution. The temperature cross-talk for tilt angle measurements is 4.08 nrad /°C, which is small compared with the resolution of the inclinometer. The prototype inclinometer was also used for monitoring variations in the tilt angle of a windowsill caused by temperature changes during a five-day period, and it demonstrated excellent robustness, stability, and practicality. The sensitivity and dynamic range of the inclinometer can be flexibly configured by simply changing the length of the rope. The resolution of 20 nrad that we achieved with our inclinometer provides opportunities to use the novel device for investigating subtle distortions in gravitational fields.

REFERENCES

[1] Y.-T. Ho, A.-B. Huang, and J.-T. Lee, "Development of a fibre Bragg grating sensored ground movement monitoring system," Meas. Sci. Technol. 17(7), 1733 (2006).

[2] H.-F. Pei, J.-H. Yin, H.-H. Zhu, C.-Y. Hong, W. Jin, and D.-S. Xu, "Monitoring of lateral displacements of a slope using a series of special fibre Bragg grating-based in-place inclinometers," Meas. Sci. Technol. 23(2), 025007 (2012).

[3] S. Vurpillot, G. Krueger, D. Benouaich, D. Clément, and D. Inaudi, "Vertical deflection of a pre-stressed concrete bridge obtained using deformation sensors and inclinometer measurements," ACI Struct. J. 95(5), 518-526 (1998).

[4] D. W. Ha, H. S. Park, S. W. Choi, and Y. Kim, "A wireless MEMS-based inclinometer sensor node for structural health monitoring," Sensors 13(12), 16090-16104 (2013).

[5] Y.-G. Lee, H.-K. Jang, D.-H. Kim, and C.-G. Kim, "Development of a mirror mounted fiber optic inclinometer," Sensor Actuat. A-Phys. 184, 46-52 (2012).

[6] H.-N. Li, D.-S. Li, and G.-B. Song, "Recent applications of fiber optic sensors to health monitoring in civil engineering," Eng. Struct. 26(11), 1647-1657 (2004).

[7] L.-Y. Shao and J. Albert, "Compact fiber-optic vector inclinometer," Opt. Lett. 35(7), 1034-1036 (2010).

[8] O. Frazão, R. Falate, J. Fabris, J. Santos, L. Ferreira, and F. Araújo, "Optical inclinometer based on a single long-period fiber grating combined with a fused taper," Opt. Lett. 31(20), 2960-2962 (2006).

[9] L. Amaral, O. Frazão, J. Santos, and A. L. Ribeiro, "Fiber-optic inclinometer based on taper Michelson interferometer," IEEE Sens. J. 11(9), 1811-1814 (2011).

[10] T. Osuch, K. Markowski, A. Manujło, and K. Jędrzejewski, "Coupling independent fiber optic tilt and temperature sensor based on chirped tapered fiber Bragg grating in double-pass configuration," Sensor Actuat. A-Phys. 252, 76-81 (2016).

[11] C.-L. Lee, W.-C. Shih, J.-M. Hsu, and J.-S. Horng, "Asymmetrical dual tapered fiber Mach-Zehnder interferometer for fiber-optic directional tilt sensor," Opt. Express 22(20), 24646-24654 (2014).

[12] H. Bao, X. Dong, L.-Y. Shao, C.-L. Zhao, C. Chan, and P. Shum, "Temperature-insensitive 2-D pendulum clinometer using two fiber Bragg gratings," IEEE Photonic Tech. L. 22(12), 863-865 (2010).

[13] H. Bao, X. Dong, C. Zhao, L.-Y. Shao, C. C. Chan, and P. Shum, "Temperature-insensitive FBG tilt sensor with a large measurement range," Opt. Commun. 283(6), 968-970 (2010).

[14] B.-J. Peng, Y. Zhao, Y. Zhao, and J. Yang, "Tilt sensor with FBG technology and matched FBG demodulating method," IEEE Sens. J. 6(1), 63-66 (2006).

[15] S. Liu, N. Liu, M. Hou, J. Guo, Z. Li, and P. Lu, "Direction-independent fiber inclinometer based on simplified hollow core photonic crystal fiber," Opt. Lett. 38(4), 449-451 (2013).

[16] Q. Rong, X. Qiao, T. Guo, H. Yang, Y. Du, D. Su, R. Wang, D. Feng, M. Hu, and Z. Feng, "Orientation-dependant inclinometer based on intermodal coupling of two-LP-modes in a polarization-maintaining photonic crystal fiber," Opt. Express 21(15), 17576-17585 (2013).

[17] B. P. Abbott, R. Abbott, T. Abbott, M. Abernathy, F. Acernese, K. Ackley, C. Adams, T. Adams, P. Addesso, and R. Adhikari, "Observation of gravitational waves from a binary black hole merger," Phys. Rev. Lett. 116(6), 061102 (2016).

[18] M. Schmidt, B. Werther, N. Fürstenau, M. Matthias, and T. Melz, "Fiber-Optic Extrinsic Fabry-Perot Interferometer Strain Sensor with< 50 pm displacement resolution using three-wavelength digital phase demodulation," Opt. Express 8(8), 475-480 (2001).

[19] Y. Huang, T. Wei, Z. Zhou, Y. Zhang, G. Chen, and H. Xiao, "An extrinsic Fabry–Perot interferometer-based large strain sensor with high resolution," Meas. Sci. Technol. 21(10), 105308 (2010).

[20] B. H. Lee, Y. H. Kim, K. S. Park, J. B. Eom, M. J. Kim, B. S. Rho, and H. Y. Choi, "Interferometric fiber optic sensors," Sensors 12(3), 2467-2486 (2012).

[21] C. Zhu, Y. Chen, Y. Du, Y. Zhuang, F. Liu, R. E. Gerald, and J. Huang, "A Displacement Sensor With Centimeter Dynamic Range and Submicrometer Resolution Based on an Optical Interferometer," IEEE Sens. J. 17(17), 5523-5528 (2017).

[22] Y. Du, Y. Chen, C. Zhu, Y. Zhuang, and J. Huang, "An embeddable optical strain gauge based on a buckled beam," Rev. Sci. Instrum. 88(11), 115002 (2017).

[23] C. Zhu, Y. Chen, Y. Zhuang, Y. Du, R. Gerald, Y. Tang, and J. Huang, "An Optical Interferometric Triaxial Displacement Sensor for Structural Health Monitoring: Characterization of Sliding and Debonding for a Delamination Process," Sensors 17(11), 2696 (2017).

[24] Y. Du, Y. Chen, Y. Zhuang, C. Zhu, F. Tang, and J. Huang, "Probing Nanostrain via a Mechanically Designed Optical Fiber Interferometer," IEEE Photonic Tech. L. 29(16), 1348-1351 (2017).

[25] Wunderground.com, "Rolla, MO Forecast | weather underground ", retrieved October 25th, 2017, https://www.wunderground.com/weather/us/mo/rolla/65401.

II. A HIGH-RESOLUTION TWO-DIMENSIONAL FIBER OPTIC INCLINOMETER FOR STRUCTURAL HEALTH MONITORING APPLICATIONS

Yiyang Zhuang[1], Yizheng Chen[1], Chen Zhu, Rex E. Gerald II, Yan Tang, and Jie Huang*

Deparment of Electrical and Computer Engineering, Missouri University of Science and Technology, Rolla, MO 65409

[1] These authors contributed equally to this work.

*jieh@mst.edu

ABSTRACT

We report and demonstrate a high-resolution extrinsic Fabry-Perot interferometer (EFPI)-based two-dimensional (2-D) fiber optic inclinometer for tilt measurements in two orthogonal dimensions. The inclinometer consists of a pair of perpendicularly-arranged EFPI sensors packaged inside a rectangular container box. A triangular-shaped metal prism is attached to the top plate of the container box by three ropes with identical lengths. Two optical fibers are rigidly connected to the top plate of the container box by two supporting rods, respectively. Therefore, two EFPI sensors are formed between the endfaces of two optical fibers and their corresponding side face mirrors. The prism is connected to a cross paddle, which is immersed in a damping fluid to reduce the influence of deleterious vibrations. After tilting, the two reflectors of each EFPI sensor will remain parallel while the cavity lengths of the EFPI sensors change. Changes in the cavity lengths can be calculated, and the 2-D tilt angles of the inclinometer can be calculated according to the Fabry-Perot principle. The design of the sensor and the measurement principles are discussed. Measurements of the tilt angles of a simply-supported beam induced by small loads are presented to verify the tip-angle resolution and uncertainty of the two EFPI sensors in our 2-D inclinometer. The results show the capability for metering tilt angles with high resolution. The 2-D inclinometer was used to continuously monitor the tilt angle of a gravity dam for a one-year period, showing excellent stability and practicability.

Keywords: Two-dimensional inclinometer, Fiber optic sensor, Fabry-Perot interferometer, Structural health monitoring, Pendulum

1. INTRODUCTION

Inclinometers purposed for tilt measurements have attracted considerable attention for structural health monitoring and warning of impending natural disasters such as landslides and earthquakes [1-3]. The concept behind a typical inclinometer is that it measures variations in tilt angles generated by the behavior of a pendulum subject to a gravitational field [4].

For several applications in harsh environments, the inclinometers require high resolution and long durations of continuous operation to precisely monitor the variations in the tilt. Furthermore, for certain applications, inclinometers must function in dangerous and isolated places, requiring capabilities such as long-distance lossless transmission, non-electromagnetic interference, resistance to hazardous environments, etc.[5].

Fiber optic sensors are promising candidates for inclinometers owing to their unique advantages such as immunity to electromagnetic interference, low transmission loss, high accuracy, the possibility of remote operation, and robustness when compared with conventional electrolytic inclinometers [6]. In recent years, a variety of fiber optic inclinometers have been reported and developed [7-21]. The sensing principles of the majority of the reported fiber-optic inclinometers are based on wavelength or intensity modulations of the input signals caused by bending the fiber optic sensors. Examples include fiber tapers [7-11], fiber Bragg gratings (FBG) [13], photonic crystal fiber-based devices [16-18] and grating-based devices [5, 19]. However, most of the reported fiber-optic inclinometers can only distinguish the magnitude, but not the direction of inclination. A common solution for two-dimensional (2-D) inclination measurements is to combine two or more inclinometers to independently measure the inclination in two orthogonal directions [12, 14, 15]. Recently, a few 2-D fiber-optic inclinometers were reported. Au et al. demonstrated a large dynamic range tilt sensor consisting of four FBGs inscribed on a fiber-cross and a central mass, which achieved a ±30° dynamic range and a 0.013° resolution [14]. Bao et al. proposed a temperature-insensitive 2-D inclinometer by attaching two FBGs, orthogonally, on a tapered cylindrical beam, which achieved a 2-D tilt measurement of over a ±4° dynamic range and a 0.027° resolution [15]. Chang et al. developed their 2-D inclinometer with a 0.003° tilt angle resolution based on two etched chirped-FBG arrays installed in close proximity and placed in a container filled with diethyl-ether and an air bubble [20]. Chen et al. reported a 2-D inclinometer with a 2.5° dynamic range in which three ultraweak FBGs were interrogated with coherent optical frequency-domain reflectometry and were bound together using a thermoformed plastic [21]. However, all of the aforementioned fiber-optic 2-D inclinometers suffer from debonding between the fiber-optic sensors and the corresponding tilt-angle transducers, which affected the long-term stability of the inclinometers. Also, the specified resolutions for all of the aforementioned fiber-optic inclinometers are in the range of microradians to milliradians [7-21], which is not sufficient for some applications in aerospace engineering and gravitational field measurements, where extremely small-angle tilt measurements are required [22].

A widely used interferometric sensor, the extrinsic Fabry-Perot interferometer (EFPI), has the merits of displacement and strain measurements [23-28]. An EFPI is generally formed by the endface of an optical fiber and an external reflecting surface, which enhances the flexibility of sensor designs. Moreover, the cavity length of the EFPI (i.e., the distance between the two reflecting surfaces) can be precisely measured from the reflection spectrum [25]. Therefore, with proper structure designs and packaging, EFPI sensors could be used for tilt measurements. Recently, we reported a 1-D high-resolution EFPI-based fiber optic inclinometer [29]. And, Yang et al. also reported a fiber-optic Fabry-Perot sensor for tilt-angle and vibration measurements with a similar structure [30]. However, simply combining any two 1-D inclinometers presents significant challenges such as cross-talk that arises from inaccurate assembly.

In this paper, we report and demonstrate a high resolution EFPI-based 2-D fiber optic inclinometer for simultaneous tilt angle measurements in two orthogonal dimensions that minimizes cross-talk errors by an integrated orthogonal design. The demonstrated inclinometer consists of a pair of perpendicularly-arranged EFPI sensors packaged inside a rectangular metal container box. The sensor design and the measurement principle are discussed. An experiment based on measuring the mutually-orthogonal tilt angles of a simply-supported beam caused by small load increments (2.000g) is presented to verify the resolution of the 2-D inclinometer. A resolution of 20 nrad was achieved. The 2-D inclinometer was also used to continuously monitor orthogonal tilt angles of a gravity dam throughout one year.

2. SENSOR DESIGN AND MEASUREMENT PRINCIPLE

A schematic diagram of the 2-D inclinometer is illustrated in Figure 1(a). A pair of perpendicularly arranged EFPI sensors are assembled and packaged in a rectangular container box fabricated of Invar metal (Figure 1(b)). The EFPI sensors consist of two parts: the metal prism part and the optical fiber part. As for the metal prism part, a right triangle metal prism is flexibly connected to the top plate of the container box by three steel strand ropes of the same length. Two side face mirrors of the prism are perpendicular to each other, which are defined as S_1 and S_2 in Figure 1(a). The three connection ropes are shown in Figure 1(a) and labeled AA', BB', and CC', where A, B, and C are the connection points on the top plate of the container box and A', B', and C' are the connection points on the top face of the metal prism. The distance between the connection points of any two ropes on the top plate of the container box and the corresponding top face of the metal prism are equal (i.e., AB=A'B', BC=B'C', and AC=A'C'). Thus, the top plate of the container box will always be parallel to the top face of the metal prism. For convenience, we define the coordinate system where the x, y, and z-axes are perpendicular to S_2, S_1, and the top face of the metal prism, respectively. As for the optical fiber components, two optical fibers are rigidly connected to the top plate of the container box by two supporting rods. The supporting rods are perpendicular to the top plate of the container box. And, the endfaces of the two optical fibers OF_1 and OF_2 are precisely adjusted to be parallel to S_1

and S_2, respectively. Therefore, two EFPI sensors ($EFPI_1$ and $EFPI_2$) with air-gap cavities are formed by S_1, S_2, and the two corresponding endfaces of the two optical fibers OF_1 and OF_2, respectively. Also, both S_1 and S_2 are coated with a thin layer of gold to increase the reflectivity of the respective mirror surfaces. The 2-D inclinometer is equipped with a vibration reduction device. A cross paddle is rigidly connected to the bottom of the metal prism by a metal rod and it is immersed into a damping fluid. When the inclinometer experience a vibration, the moving of the cross paddle will be damped by the damping fluid, which can physically reduce vibrations of the metal prism. Alternatively, vibration reduction can also be achieved by a magnetic mechanism (e.g., a combination of electromagnets and/or magnets). And the perspective view of the assembly figure of the inclinometer is shown in Figure 1(b). Two optical fiber connectors were fixed inside the through holes which were drilled through each supporting rod. The lead-out optical fibers, via the channels on the top of the container box, were connected to the interrogation system. After assembly of the inclinometer, the damping fluid was filled into the 2-D inclinometer fluid reservoir through a small porthole located on the top of the container box. Figure 1(c) is a photograph of a prototype 2-D inclinometer.

The yz-plane side views of the 2-D inclinometer before and after tilting are illustrated in Figure 2(a) and Figure 2(b), respectively, to explicitly demonstrate the measurement principle. S_1 and the endface of the corresponding optical fiber OF_1 serve as the two reflectors of $EFPI_1$. When the inclinometer is tilted at an angle θ (see Figure 2(b)), the two ropes (AA' and BB') will remain perpendicular to the horizontal ground plane due to the gravitational field. Meanwhile, the OF supporting rod will be tilted with the inclinometer, and the angle between the OF supporting rod and the ropes is the tilt angle

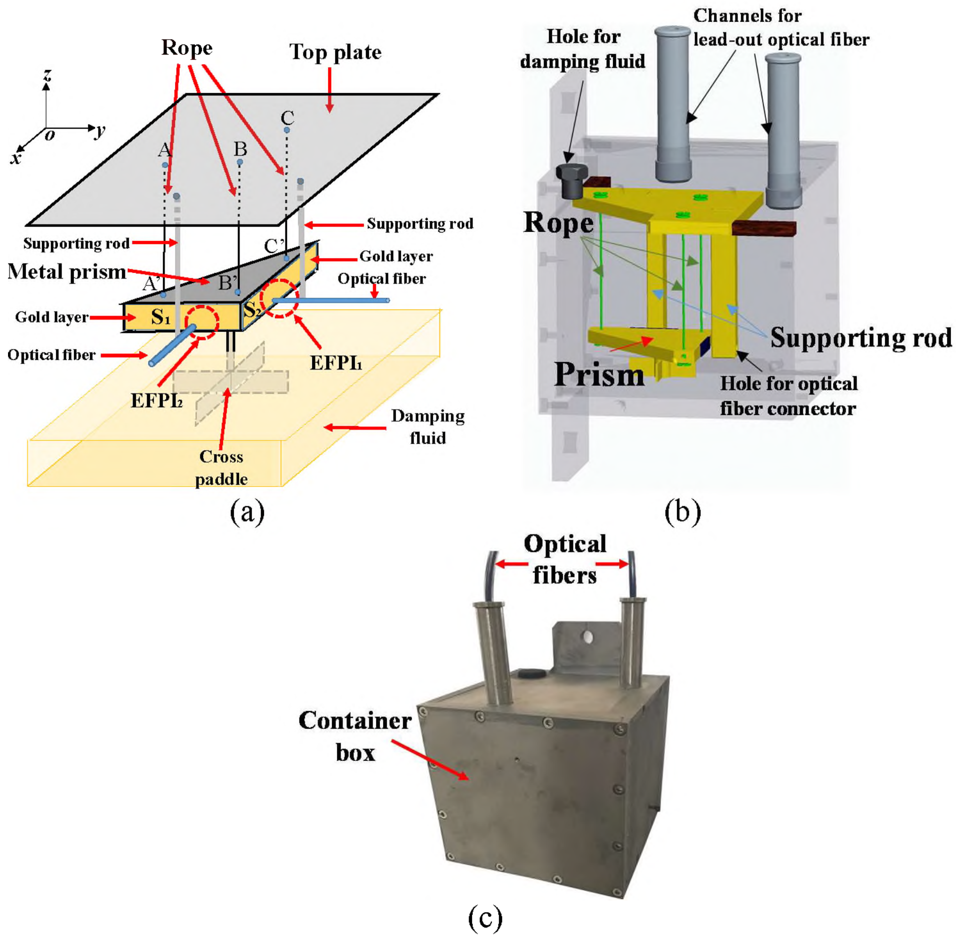

Figure. 1. Schematic diagram and photograph of the 2-D inclinometer described in this work. (a) Schematic diagram of the inclinometer. A triangular metal prism is flexibly connected to the top plate of the rectangular metal container box by three ropes of the same length (AA', BB', and CC'). Two optical fibers are rigidly connected to the top plate of the container box using supporting rods. Two EFPI sensors are formed between the endfaces of the optical fibers (OF_1 and OF_2) and two corresponding side face mirrors (S_1 and S_2) of the metal prism. S_1 and S_2 are coated with gold to form highly reflective mirror surfaces. The vibration reduction device consists of a cross paddle connected to the metal prism, which is immersed in a damping fluid. The cross paddle remains submerged in the damping fluid for the range of tilt angles metered by the inclinometer. (b) Perspective view of the assembly figure of the 2-D inclinometer. (c) Photograph of a prototype 2-D inclinometer. Two optical fiber connectors were fixed inside the through holes which were drilled through each supporting rod. The lead-out optical fibers via the channels on the top of the container box will be connected to the interrogation system. After inclinometer assembling, the damping fluid will be filled into the 2-D inclinometer through a small hole on the top of the container box.

of the inclinometer. The metal prism will remain parallel to the top plate of the container box because the four connection points (A, A', B, and B') form a parallelogram. As a result, the two reflectors of $EFPI_1$ will remain parallel, but the distance between the two reflectors, the cavity length of $EFPI_1$, will change. The relative position of the 2-D inclinometer before tilting is shown in Figure 2(b) with a dashed outline, while the position of the 2-D inclinometer after tilting is represented with a solid outline. Figure 2(b) clearly shows the change in the position of S_1.

$EFPI_2$ shares a common measurement principle with $EFPI_1$. Since S_1 and S_2 are perpendicular to each other, the cavity length of $EFPI_1$ will only be influenced by the tilt in the yz-plane, or the y-dimension, while the cavity length of $EFPI_2$ will only be influenced by the tilt in the xz-plane, or the x-dimension. The tilt angle of the 2-D inclinometer in the yz-plane, $\Delta\theta_1$, can be described as follows:

$$\Delta\theta_1 = \arcsin\frac{\Delta d_1}{l} \tag{8}$$

where Δd_1 is the change in the cavity length of $EFPI_1$ and l is the length of each of the steel strand ropes. When the tilt angle is small, (1) can be described as:

$$\Delta\theta_1 = \arcsin\frac{\Delta d_1}{l} \approx \frac{\Delta d_1}{l} \tag{9}$$

Similarly, the tilt angle of the 2-D inclinometer in the xz-plane, $\Delta\theta_2$, (the x-dimension) can be described as follow:

$$\Delta\theta_2 = \arcsin\frac{\Delta d_2}{l} \tag{10}$$

And,

$$\Delta\theta_2 \approx \frac{\Delta d_2}{l} \tag{11}$$

when the tilt angle is small, where Δd_2 is the change in the cavity length of $EFPI_2$. Here, both $\Delta\theta_1$ and $\Delta\theta_2$ can be positive or negative corresponding to counterclockwise or clockwise tilts, respectively. When the applied tilt angle is relatively small (i.e., under mrad), the difference between tilt angle calculations using (1) and (2) (or (3) and (4)) is less than 0.001%. And the relationship between tilt angle change and cavity length change can be considered as linear, which indicates that the 2-D inclinometer is able to keep the same sensitivity in a small measurement range.

As mentioned above, the endfaces of the corresponding optical fibers, together with S_1 and S_2 form two EFPI sensors with a cavity length of d_1 and d_2, respectively. Considering $EFPI_1$ as an example, the interference signal (I_{E1}) of $EFPI_1$ is given by

$$I_{E1} = I_1 + I_2 + 2\sqrt{I_1 I_2}\cos(\frac{4\pi n d_1}{\lambda} + \varphi) \tag{12}$$

where I_1 and I_2 are the light intensities reflected from the endface of the optical fiber and the corresponding mirror endface of the metal prism, respectively, φ is the initial phase difference between two reflected waves, n is the refractive index of air, which is about 1, and λ is the wavelength of the incident light. When the variables inside the cosine function of (5) are equal to a multiple of 2π, constructive interferences result. In the wavelength spectrum of the interference signal, the separation between two adjacent peaks, defined as the free spectrum range (FSR), can be expressed as:

$$FSR = \frac{\lambda_c^{\ 2}}{2d_1} \tag{13}$$

where λ_c is the center wavelength of the interference spectrum. So, the cavity length can be demodulated by determining the FSR of the interference spectrum. When the inclinometer is tilted, the cavity lengths of the EFPIs will change. The change in cavity length for $EFPI_1$ can be determined by:

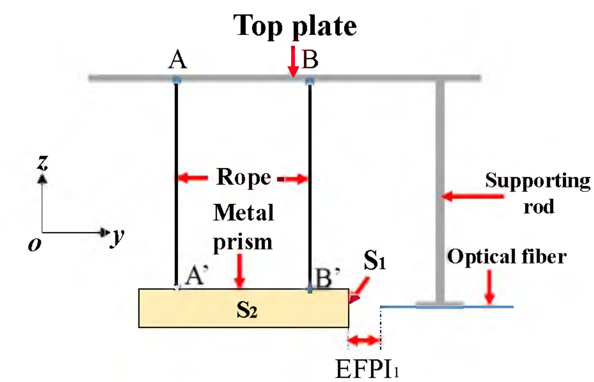

(a)

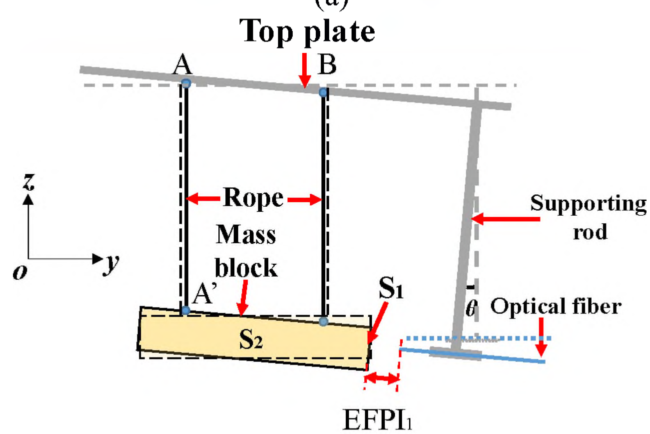

(b)

Figure 2. The yz-plane side views of the 2-D inclinometer depicting the relationship between the tilt angle θ and the length of the cavity of $EFPI_1$. (a) The yz-plane side view of the 2-D inclinometer before tilting. $EFPI_1$ is formed by S_1 and the endface of the corresponding optical fiber. (b) The side view of the 2-D inclinometer after tilting to an angle θ. The figure with the dashed outline shows the relative position of the 2-D inclinometer before tilting, while the figure with a solid outline shows the position of the 2-D inclinometer after tilting. S_1 remains parallel to the endface of the corresponding optical fiber, but the distance between S_1 and the endface of the optical fiber (i.e., the cavity length of $EFPI_1$) changes upon tilting.

$$\Delta d_1 = \frac{\lambda_c^{\ 2} \Delta FSR_{E1}}{2 FSR_{E10} FSR_{E11}} \tag{14}$$

where FSR_{E10} and FSR_{E11} are the values of FSR for $EFPI_1$ before and after tilting, respectively; ΔFSR_{E1} is the difference between FSR_{E10} and FSR_{E11}. The sign of ΔFSR_{E1} can be used to determine the direction of tilt. For example, in Figure 2(b), if the metal prism part tilts clockwise, then the cavity length of $EFPI_1$ experiences a decrease. And, if the metal prism part tilts counterclockwise, then the cavity length of $EFPI_1$ experiences an increase.

Similarly, for $EFPI_2$, the cavity length change Δd_2 can be determined by:

$$\Delta d_2 = \frac{\lambda_c^2 \Delta FSR_{E2}}{2FSR_{E20}FSR_{E21}} \tag{15}$$

where FSR_{E20}, FSR_{E21}, and ΔFSR_{E2} are the values of FSR for $EFPI_2$ before tilting, after tilting, and the difference between FSR_{E20} and FSR_{E21}, respectively.

With reference to the demodulation principle shown above, changes of the cavity lengths of the two EFPIs can be determined. It should be noted that no matter how much the tilt angle is (within the operational range of the inclinometer), the endfaces of the two optical fibers will always be parallel to the corresponding reflective side face mirrors of the metal prism. Thus, the tilt angles can be measured if the cavity length is within a proper range (i.e., the cavity lengths of both EFPIs are less than 1 mm). More significantly, the sensitivity and the measurement range of the inclinometer are user-configurable by adjusting the rope lengths. Thus, the requirements for different practical applications can be satisfied using appropriate design parameters. For example, with a 500 μm initial cavity length and 6 cm rope lengths, the theoretical sensitivity and measurement range can be calculated to be 60 nm/μrad (cavity length change/tilt angle change) and -8.333 mrad to 8.333 mrad, respectively.

In addition, to reduce the temperature cross-sensitivity of the inclinometer, all of the rigid components of the inclinometer, including the metal prism, the supporting rods, and the container box, were made of Invar metal, which has a low coefficient of thermal expansion. Sharing a similar sensor structure with our previously proposed 1-D inclinometer, the temperature cross-talks of the 2-D inclinometer can be described as [29]

$$\Delta d_{t1} = \left(d_1\alpha_{CTE1} + l\theta\alpha_{CTE2}\right)\Delta T \tag{9}$$

$$\Delta d_{t2} = \left(d_2\alpha_{CTE1} + l\theta\alpha_{CTE2}\right)\Delta T \tag{10}$$

where ΔT is the temperature change experienced by the inclinometer; θ is the tilt angle of the inclinometer from the perpendicular line; α_{CTE1} and α_{CTE2} are the coefficients of thermal expansion of Invar and Nylon, respectively. The sensitivity to temperature cross-talk can be further reduced by selecting different materials for the metal prism and top plate so that the thermal-induced mechanical changes can be canceled out completely.

3. EXPERIMENTAL RESULTS AND DISCUSSIONS

To verify the resolution of the prototype 2-D inclinometer, an experiment based on measuring the tilt angle at the support line of a simply-supported beam under external load was designed and demonstrated. The schematic diagram of the test experiment setup is illustrated in figure 3(a). The beam was made of stainless steel. The size of the beam was 700 mm×50 mm×8 mm. The distance between each support line and the corresponding end of the beam was 100 mm. Thus, the effective length of the beam (i.e., the distance between the support lines) was 500 mm. The 2-D inclinometer was placed at the position

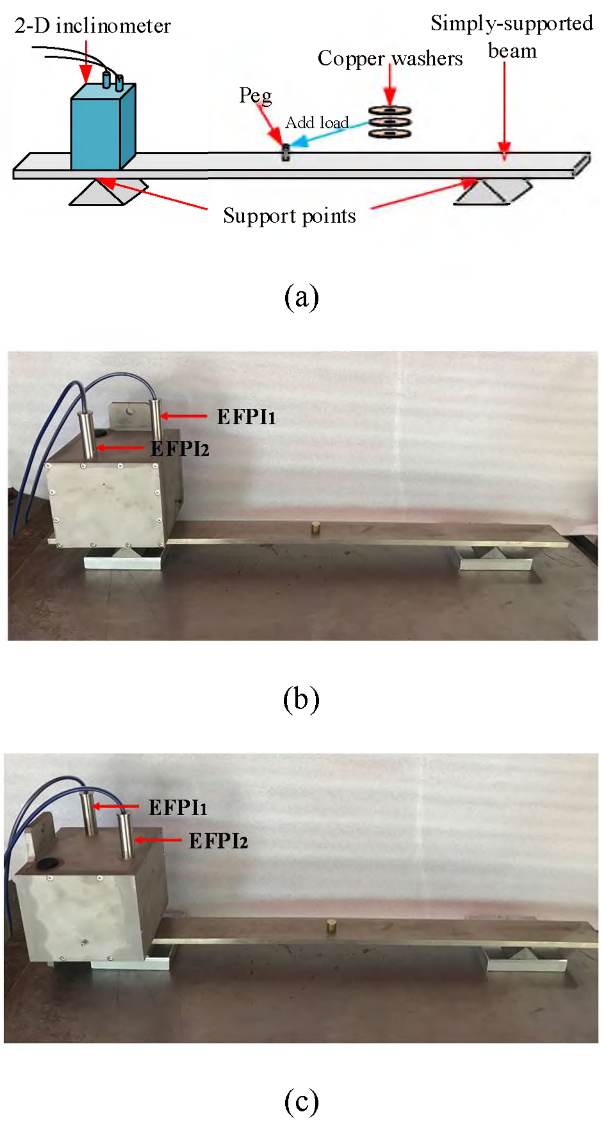

Figure 3. Schematic diagram and photographs of the 2-D inclinometer tilt angle measurement experiment apparatus, which is based on a simply-supported beam. (a) The inclinometer is placed above the position of the left-side support line. Copper washers are used to provide the load for (bending) tilting the beam. Two EFPI sensors inside the 2-D inclinometer are separately tested by rotating the 2-D inclinometer by 90 degrees between test experiments. (b) A photograph of the experiment setup when testing $EFPI_1$. (c) A photograph of the experiment setup when testing $EFPI_2$.

above one of the support lines. Several copper washers were placed on the center point of the beam to provide the necessary load to bend the beam and thereby tilt the beam at the support lines. To prevent the copper washers from sliding, a peg was soldered at the center point of the beam, and each copper washer was fabricated with a small center hole so it could be fixed on the peg. To calibrate the responses for two EFPI sensors separately, the 2-D inclinometer was rotated and adjusted so that only one EFPI was parallel to the tilt direction for each test. Photographs of the experiment setup used for calibrating $EFPI_1$ and $EFPI_2$ are shown in Figure 3(b) and Figure 3(c), respectively.

At the support line, the tilt angle can be expressed as [31]:

$$\theta = \frac{Fl_s^2}{16EI} \tag{11}$$

where F is the load applied to the center of the beam; l_s is the distance between the two support lines; E is Young's modulus for stainless steel (about 200 GPa); and, I is the moment of inertia. Note that the change in the angle calculated using (9) has uncertainty due only to the uncertainty in the change in mass that is added onto the center of the simply-supported beam (±0.001 g). Uncertainties in the other variables in (9) result in an offset angle that can be arbitrarily adjusted to zero.

The schematic test measurement setup of the 2-D interferometer apparatus for operating the 2-D inclinometer and a photograph of the 2-D inclinometer are shown in Figure 4. A wavelength interrogator (Micron Optics SM125) served as the light source and demodulation device for the 2-D interferometer apparatus. The interference spectra of both EFPI sensors were recorded separately using an optical switch. A detailed description of the measurement apparatus can be found in our recent work [32].

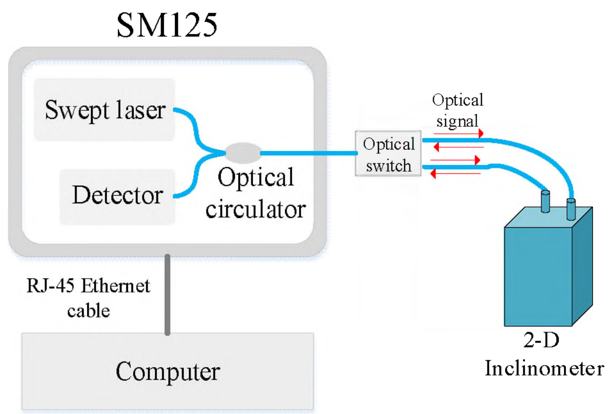

Figure 4. Schematic diagram of the test measurement setup for operating the 2-D inclinometer and a photograph of the 2-D inclinometer. A computer-controlled optical switch was used to switch between the two tilt sensors.

Figure 5(a) and Figure 5(b) shows the interference spectrum of $EFPI_1$ and $EFPI_2$, respectively without tilting the inclinometer. The averaged FSR of the $EFPI_1$ and the $EFPI_2$ spectrum is 4.205 nm and 5.030 nm, corresponding to the initial cavity length of 285.680 µm and 238.825 µm, respectively. And, the dynamic range boundaries of $EFPI_1$ and $EFPI_2$ were calculated to be -4.761 mrad to 11.905 mrad (-0.273° to 0.682°) and -3.980 mrad to 12.686 mrad (-0.228° to 0.727°), respectively. It should be noted that the differences in FSR values of both EFPIs will only result in different initial cavity lengths instead of different coupling efficiencies or sensitivities. In our experiments, the cavity lengths for both EFPI sensors were measured for 55 minutes. During the measurements, for each load, five interference spectra were recorded to calculate the cavity length of each EFPI sensor. During the experiment, each EFPI sensor of the inclinometer was interrogated separately by switching channels, and the spectra from the EFPI sensor, which was not under test, were also recorded to investigate the error introduced by the orthogonal fabrication of the 2-D inclinometer and the configuration of the experimental setup. The weight of each copper washer was 2.000±0.001g. According to (2) and (4), when a copper washer was placed on the center point of the beam, it would cause a tilt angle to the beam of 0.757 μrad. The total load ranged from 0 to 20.000 g corresponded to the range in tilt angle from 0 to 7.570 μrad.

For the test experiment of $EFPI_1$, the changes in the cavity lengths of $EFPI_1$ as a function of applied loads (parameterized with a time variable) are shown in Figure 6(a). The left vertical axis represents the changes in the measured cavity lengths of the $EFPI_1$ sensor, and the right vertical axis represents the corresponding measured tilt angle changes, which were calculated from (2) with the length of the rope set to 6.000 cm in the prototype 2-D inclinometer. In Figure 6(a), a load increment of 2.000 g placed on the center point of the simply-supported beam, corresponding to an increment of 0.757 μrad in the tilt angles, can be easily metered by $EFPI_1$. The measurement setup, based on the SM125, can achieve a resolution of 1.0 nm for changes in lengths of the EFPI cavity.

Thus, the EFPI-based inclinometer described here can achieve a theoretical resolution of 16.7 nrad according to (2). The deviations of the changes of the measured cavity lengths from the average change and the corresponding deviations of the changes of the tilt angles form the average change during the measurement period 35-40 min are presented as an inset in Figure 6(a), showing a standard deviation of 0.008 μrad. The changes in the cavity lengths of $EFPI_2$ as a function of applied loads (parameterized with a time variable) are shown in Figure 6(b). The changes in the cavity lengths follow an increasing trend with load increments. An inset showing the changes in the cavity lengths measured during the measurement period 31-35 min is also presented in Figure 6(b) to

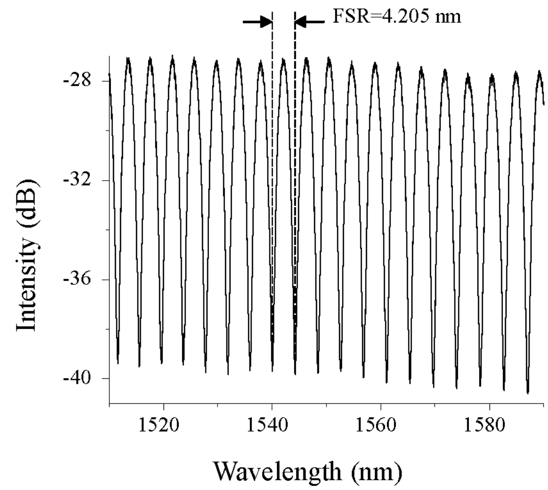

(a)

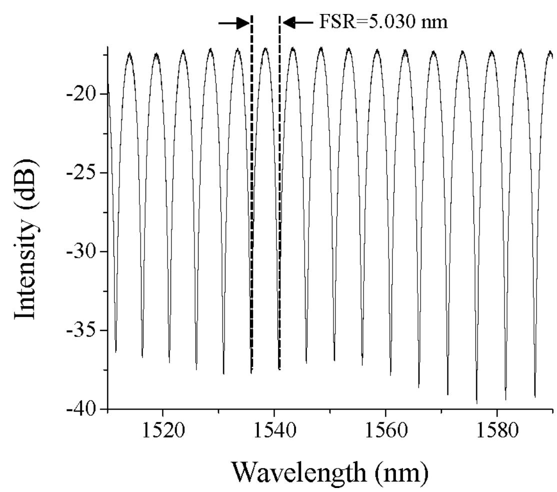

(b)

Figure 5. Initial interference spectra from two orthogonal EFPI sensors. (a) Initial interference spectrum from $EFPI_1$. The spectrum was recorded from 1510 nm to 1590 nm. The average FSR of $EFPI_1$ is 4.205 nm, corresponding to a cavity length of 285.680 μm. (b) Initial interference spectrum from $EFPI_2$. The spectrum was recorded from 1510 nm to 1590 nm. The average FSR of $EFPI_2$ is 5.030 nm, corresponding to a cavity length of 238.825 μm.

show the standard deviation of the corresponding measured cross-talk angles, which is 0.010 μrad. The measured tilt angles from $EFPI_1$ and the cross-talk angles from $EFPI_2$ plotted as a function of applied tilt angles, calculated according to (2) and (4), are shown

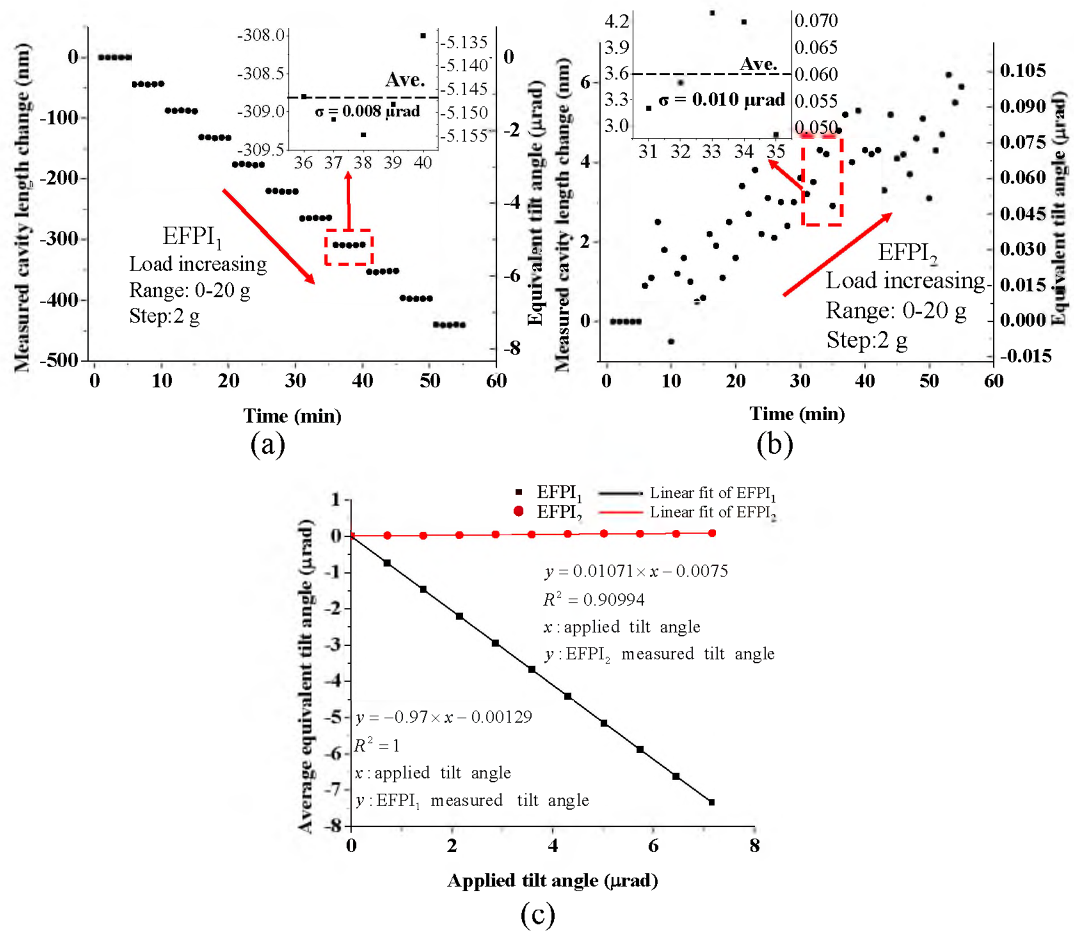

Figure 6. Tilt and cross-talk angle measurement results for a simply-supported steel beam using the 2-D inclinometer. (a) Plot of the changes in cavity lengths and the corresponding changes in the measured tilt angles as a function of applied loads from $EFPI_1$. Every five minutes the load was increased by 2.000 g and every minute the interference spectrum was recorded. The inset shows the changes in the cavity lengths and the corresponding measured tilt angles for measurement times that spanned from 36 to 40 minutes. (b) Plot of the cross-talk angle experimental results obtained from $EFPI_2$. The changes in the cavity lengths and the corresponding measured changes in the cross-talk angles of $EFPI_2$ are plotted as a function of applied loads. The inset shows the changes in cavity lengths and the corresponding measured changes in the cross-talk angles for measurement times that spanned from 31 to 35 minutes. (c) The average changes in the measured tilt angles from $EFPI_1$ and the average changes in the measured cross-talk angles from $EFPI_2$ as a function of the applied angles. The linear fit result of $EFPI_1$ indicates good linearity between the changes in the measured tilt angles of $EFPI_1$ and the changes in the applied tilt angles. The linearity between the changes in the measured cross-talk angles of $EFPI_2$ and the changes in the applied tilt angles is an indication that $EFPI_2$ is not perfectly orthogonal to the tilt direction of the simply-supported beam, or that the mirrors S_1 and S_2 are not perfectly orthogonal, or that the beam experiences a twist under load, or a combination of these reasons.

in Figure 6(c). The linear fit (black line) of the data collected with $EFPI_1$ produces an R-square of 1, indicating the excellent linearity between the applied tilt angles (derived from the placement of the copper washers on the center point of the beam) and measured tilt angles. The slope and the intercept of the linear fit result reveal the differences between the applied tilt angles and measured tilt angles. The reason for the small differences could be ascribed to the parameters used to calculate the tilt angles of the beam (e.g., Young's modulus of steel, the length of the steel beam, etc.). However, the differences can be compensated using the linear fit results. On the other hand, the linear fit (red line) of the data collected with $EFPI_2$ resulted in an R-square of only 0.90994 because the small alignment errors introduced by the fabrication of the inclinometer and the geometrical configuration of the experimental setup are of the same order of magnitude as the deviations in tilt angle measurements. The slope of the $EFPI_2$ linear fit result indicates that the coordinate not under test also experienced small cross-talk angle changes (1.1% compared with the side under test) because of the uncertainties in the inclinometer fabrication and installation. It is also possible that the beam experiences a twist under load, which is metered as a cross-talk angle change.

The test experiment of $EFPI_2$ followed similar steps as the test experiment of $EFPI_1$. The changes of the cavity lengths of $EFPI_2$ as a function of applied loads (parameterized with a time variable) are shown in Figure 7(a). The left vertical axis represents the changes in the measured cavity lengths of $EFPI_2$, and the right vertical axis represents the corresponding measured tilt angle changes. In Figure 7(a), 0.757 μrad angle increments of the simply-supported beam can also be easily distinguished by $EFPI_2$. Using a similar measurement setup, the tilt angle measurement resolution of $EFPI_2$ is the same as for $EFPI_1$.

The deviations of the changes of the measured cavity lengths from the average change and the corresponding deviations of the changes of the tilt angles form the average change during the measurement period 31-35 min are presented as an inset in Figure 7(a), showing a standard deviation of 0.013 μrad. The changes in the cavity lengths of $EFPI_1$ as a function of applied loads (parameterized with a time variable) is shown in Figure 7(b). The changes in the cavity lengths follow a decreasing trend with load increments. An inset of the changes in the cavity lengths measured during the measurement period 36-40 min is also presented in Figure 7(b), showing a standard deviation of 0.013 μrad. The changes in the measured tilt angles of $EFPI_2$ and the changes in the measured cross-talk angles of $EFPI_1$ in the $EFPI_2$ test experiment as a function of the applied tilt angles are shown in Figure 7(c). The linear fit (red line) of $EFPI_2$ produced an R-square of 1, indicating the excellent linearity between the changes in the applied tilt angles and the changes in the measured tilt angles of $EFPI_2$. Meanwhile, the linear fit (black line) of $EFPI_1$ produced an R-square of 0.9813 because the alignment errors introduced by the fabrication of the inclinometer and the geometrical configuration of the experimental setup are of the same order of magnitude as the deviations in tilt angle measurements. The slope of the $EFPI_1$ linear fit also shows that a small tilt angle was detected by $EFPI_1$ due to uncertainties in the inclinometer installation. It is also possible that the beam experiences a twist under load, which is metered as a cross-talk angle change.

The stability of the proposed 2-D inclinometer was also investigated. The 2-D inclinometer was placed on the same simply-supported beam while no load was applied on the center of the beam. The interference spectra of both EFPIs was recorded by the

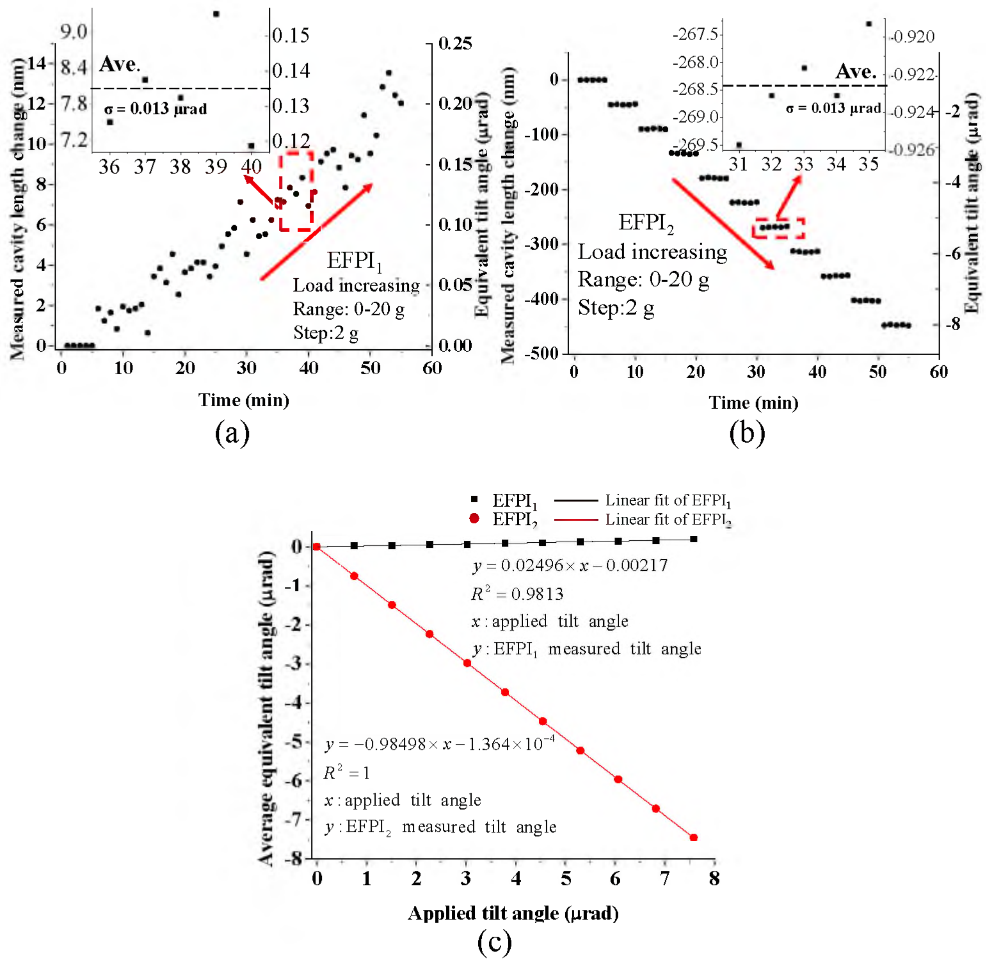

Figure 7. Tilt and cross-talk angle measurement results for a simply-supported steel beam using the 2-D inclinometer. (a) Plot of the changes in cavity lengths and the corresponding changes in the measured tilt angles as a function of applied loads from EFPI$_2$. Every five minutes the load was increased by 2.000 g and every minute the interference spectrum was recorded. The inset shows the changes in the cavity lengths and the corresponding measured tilt angles for measurement times that spanned from 31 to 35 minutes. (b) Plot of the cross-talk angle experimental results obtained from EFPI$_1$. The changes in the cavity lengths and the corresponding measured changes in the cross-talk angles of EFPI$_1$ are plotted as a function of applied loads. The inset shows the changes in cavity lengths and the corresponding measured changes in the cross-talk angles for measurement times that spanned from 36 to 40 minutes. (c) The average changes in the measured tilt angles from EFPI$_2$ and the average changes in the measured cross-talk angles from EFPI$_1$ as a function of the applied angles. The linear fit result of EFPI$_2$ indicates good linearity between the changes in the measured tilt angles of EFPI$_2$ and the changes in the applied tilt angles. The linearity between the changes in the measured cross-talk angles of EFPI$_1$ and the changes in the applied tilt angles is an indication that EFPI$_1$ is not perfectly orthogonal to the tilt direction of the simply-supported beam, or that the mirrors S_1 and S_2 are not perfectly orthogonal, or that the beam experiences a twist under load, or a combination of these reasons.

interrogator every 5 minutes. The total experiment time was 1000 minutes. The cavity length changes and their corresponding equivalent tilt angle were calculated for both EFPIs for 1000 minutes; the results are shown in Figure 8(a) and Figure 8(b). Figure 8(a) shows the recorded cavity length changes and equivalent tilt angle changes of $EFPI_1$ and Figure 8(b) shows the recorded cavity length changes and equivalent tilt angle changes of $EFPI_2$. The average and standard deviation of the cavity length change of $EFPI_1$ are calculated to be 0.03316 nm and 1.4284 nm, respectively, corresponding to a 0.55267 nrad and 23.8060 nrad equivalent change in tilt angle, respectively. The average and standard deviation of $EFPI_2$ cavity length change are calculated to be -0.20107 nm and 1.9305 nm, respectively, corresponding to -3.3511 nrad and 32.1705 nrad equivalent tilt angle change, respectively. Compared to the uncertainties in previous small tilt angle measurement, it is obvious that both EFPIs experienced larger uncertainties. The reason lies within much longer experiment time which may introduce larger environmental uncertainties. But both EFPIs still show tilting measurement standard deviations within tens of nanoradians, indicating good stability.

The temperature cross-talk of the 2-D inclinometer was investigated in a separate experiment. The experimental setup is illustrated in Figure 9(a). The inclinometer was placed inside a temperature-controlled box filled with insulation foam. To reduce the influence of the thermal expansion effect on the experimental setup, the 2-D inclinometer was placed on the top of a cylindrical fused silica base. Every hour, the temperature inside the box was increased by 10 °C. After 50 minutes for temperature stabilization, the interference signal was recorded ten times in 10 minutes. The total temperature range was

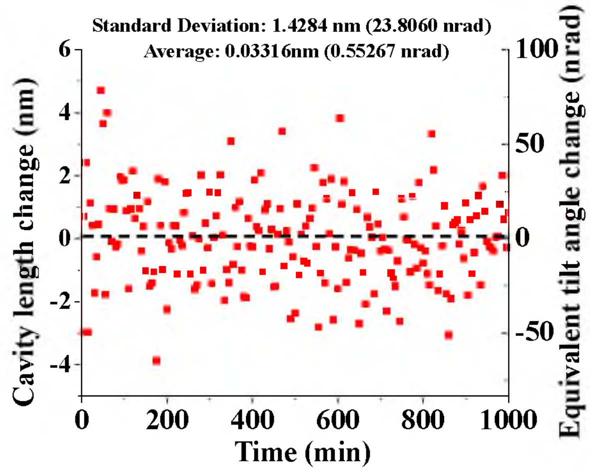

(a)

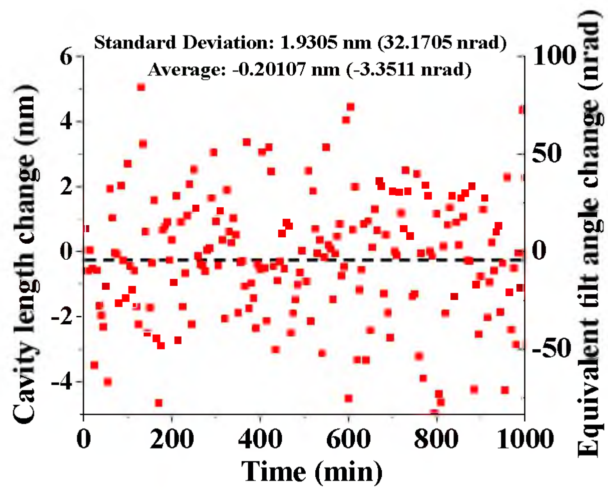

(b)

Figure 8. The stability test result for the 2D inclinometer. Every 5 minutes the interference spectra from each EFPI was recorded by the interrogator. The total experiment time was 1000 minutes. (a) The recorded cavity length changes and equivalent tilt angle changes of $EFPI_1$. (b) The recorded cavity length changes and equivalent tilt angle changes of $EFPI_2$.

0-50 °C. The initial cavity lengths of $EFPI_1$ and $EFPI_2$ were 498.376μm and 472.115 μm, corresponding to theoretical temperature cross-talks of 9.96 nrad/°C and 9.44 nrad/°C calculated from (9) and (10), respectively.

The measured $EFPI_1$ and $EFPI_2$ cavity length changes and the equivalent tilt angles as a function of temperature are shown in Figure 9(b) and Figure 9(c). Figure 9(b) and Figure 9(c) indicate that the cavity lengths of both EFPIs have a positive correlation to the temperature. The insets in Figure 9(b) and Figure 9(c) show the expanded cavity length changes and the corresponding equivalent tilt angles at a constant temperature. The standard deviations of the equivalent tilt angles derived from $EFPI_1$ and $EFPI_2$ were 40.1 nrad and 35.6 nrad, which are higher than for the previous experiments because of the larger environmental perturbations. Figure 9(d) illustrates the average equivalent tilt angles derived from $EFPI_1$ and $EFPI_2$ as a function of temperature. Based on the linear fit results of the average equivalent tilt angles derived from $EFPI_1$ and $EFPI_2$, the measured temperature cross-talks for $EFPI_1$ and $EFPI_2$ were 11.2 nrad/°C and 13.4 nrad/°C, which are close to the theoretical temperature cross-talk values. The temperature experiment results indicate that the temperature cross-talks of the inclinometer are small, and they can be reduced or compensated for by recording the effects of the temperature variations or by using proper materials for insulation from heat.

To verify the practicability of our prototype 2-D inclinometer, an experiment was conducted to monitor the tilt angle of a gravity dam (Fengman Dam, Jilin City, Jilin, China). A photograph of the gravity dam is shown in Figure 10(a). Wedefine a Cartesian coordinate system for the gravity dam where the x-direction is towards the upper reach of the river, the y-direction is along the gravity dam, and the z-direction is perpendicular to the earth. The 2-D inclinometer was located inside a vertical shaft in the 32nd section of the dam at an elevation of 258 meters above the Earth's sea level (see Figure 10(b)). The coordinate systems of the gravity dam and the 2-D inclinometer are coincident. Interference

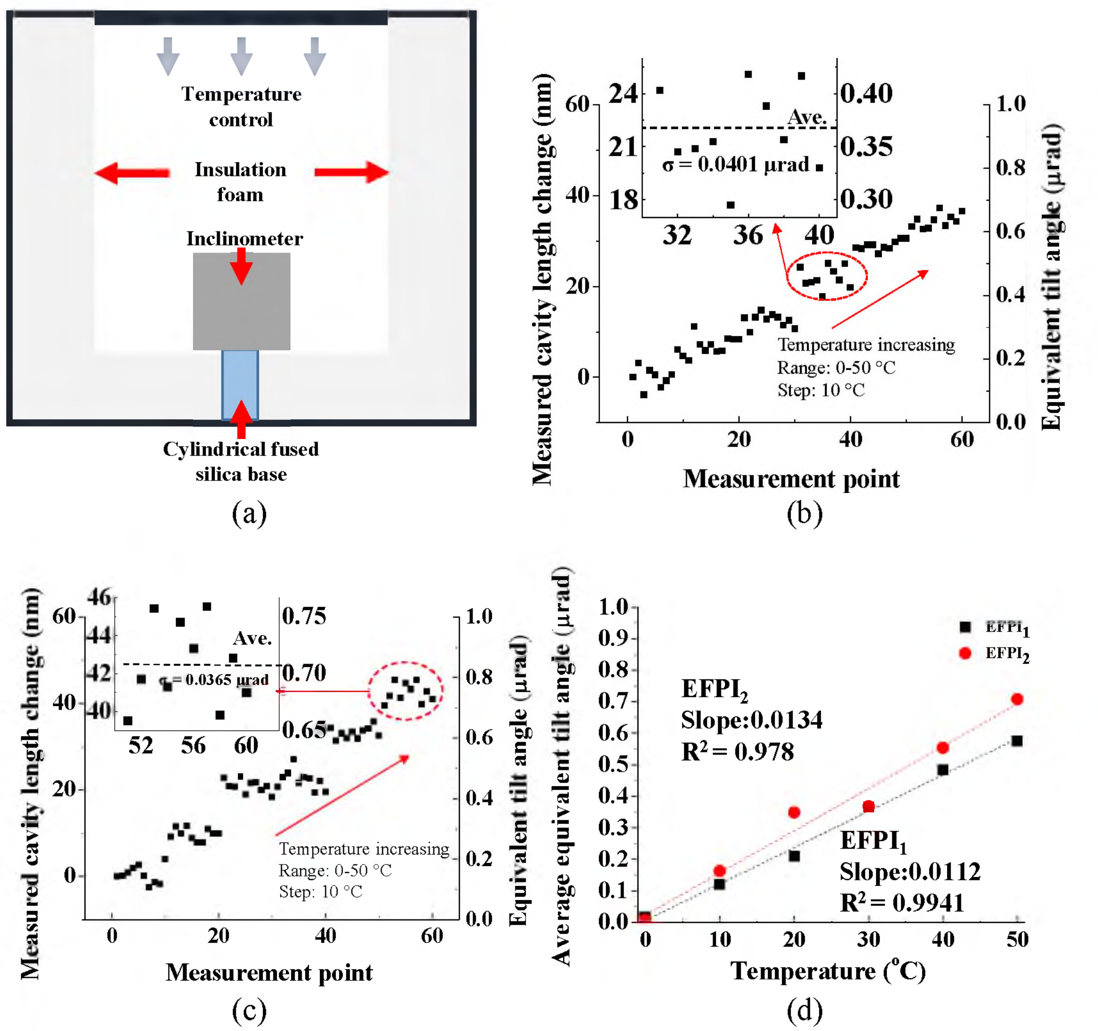

Figure 9. An experiment apparatus used to investigate the temperature cross-talk of the inclinometer and experimental results. (a) A diagram of the experimental apparatus used to quantify temperature cross-talk. The inclinometer was placed inside a temperature-controlled box surrounded with three-inch-thick insulation foam. To reduce the influence of the thermal expansion effect on the experimental setup for accurately measuring tilt angles, the 2-D inclinometer was placed on top of a cylindrical fused silica base. (b) The measured changes in the $EFPI_1$ cavity length and the corresponding equivalent tilt angles as a function of temperature. The inset shows the expanded view of the repeatedly-measured cavity length changes and the corresponding equivalent tilt angles at 30 °C. (c) The measured changes in the $EFPI_2$ cavity length and the corresponding equivalent tilt angles as a function of temperature. The inset shows the expanded view of the repeatedly-measured cavity length changes and the corresponding equivalent tilt angles at 50 °C. (d) The average equivalent tilt angles derived from $EFPI_1$ and $EFPI_2$ as a function of temperature. The measured temperature cross-talks of $EFPI_1$ and $EFPI_2$ were 11.2 nrad/°C and 13.4 nrad/°C, respectively.

spectra from the two EFPI sensors were acquired every hour and the daily average orthogonal tilt angles of the gravity dam structure perpendicular and parallel to the gravity dam were recorded for a period of one year (January 1st, 2017 to December 31st, 2017).

The changes in the orthogonal tilt angles of the gravity dam structure perpendicular and parallel to the gravity dam, measured over a period of one year, are shown in Figure 11(a) and Figure 11(b), respectively. As shown by the positive changes in the tilt angles calculated from the positive changes in the lengths of the cavity measured by $EFPI_2$ in Figure 11(a), we can conclude that the top of the gravity dam continuously tilted towards the upper reach of the river in the first 200 days of the measurement period. After that, the top of the gravity dam began to tilt towards the lower reach of the river. The latter two results are counterintuitive. Figure 11(b) shows the positive changes in the tilt angles calculated from the positive changes in the lengths of the cavity measured by $EFPI_1$, corresponding to the tilting towards the far side of the dam (where the village is located, see Figure 10(a)), as a function of time. A comparison of Figure 11(a) and Figure 11(b) indicates that the changes in the tilt angles along the river were about ten times larger than the changes in the tilt angles along the gravity dam, a reasonable result. Some relevant data of the Fengman Dam, including the average daily temperature of the dam surroundings and the water levels of the upper reach of the river and the lower reach of the river, are plotted in Figure 11(c), Figure 11(d), and Figure 11(e), respectively. Figure 11(c) shows that the average daily outdoor temperatures at the dam follow a trend similar to the curve of the changes in the measured tilt angles along the river, revealing an unexpected and strong correlation. Our hypothesis is that this phenomenon is caused by the uneven thermal expansion/contraction between two sides of the dam. The side of the dam towards the upper

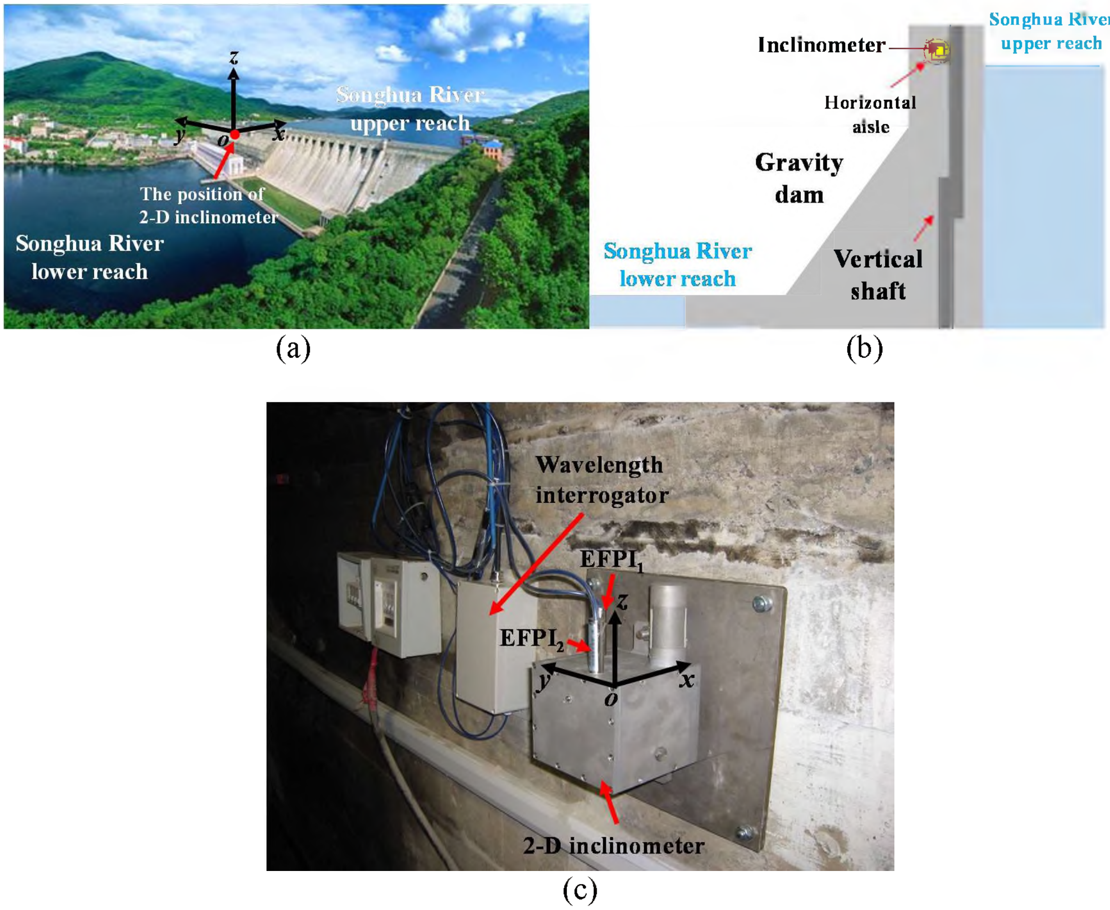

Figure 10. The photographs of the Fengman Dam, a schematic drawing of the dam, and the installed 2-D inclinometer. (a) A photograph of the Fengman Dam. The Cartesian coordinate system for the Fengman Dam is shown in the figure, which is defined such that the x-direction is towards the upper reach of the river, the y-direction is along the gravity dam, and the z-direction is perpendicular to the earth. The 2-D inclinometer was placed near the top of the dam such that the coordinate systems of the dam and the 2-D inclinometer were made coincident. (b) A cross-section schematic drawing of the 32nd dam section of the Fengman Dam. The 2-D inclinometer was located inside the horizontal aisle near the vertical shaft (yellow indicator). (c) A photograph of the 2-D inclinometer and relevant coordinate system. The 2-D inclinometer was set inside the Fengman Dam and measured the changes in orthogonal tilt angles of the Fengman Dam for one year. The Cartesian coordinate systems shown in Figure 8(a), Figure 8(b) and Figure 8(c) are the same.

reach of the river is mostly immersed in the river water, while the side of the dam towards the lower reach of the river is mostly exposed to the ambient air. Therefore, the side of the dam towards the lower reach of the river tends to experience larger temperature changes compared with the side of the dam towards the upper reach of the river, which could result in uneven thermal expansion/contraction between two sides of the dam. When the environmental temperature increases, the side of the dam towards the lower reach of the

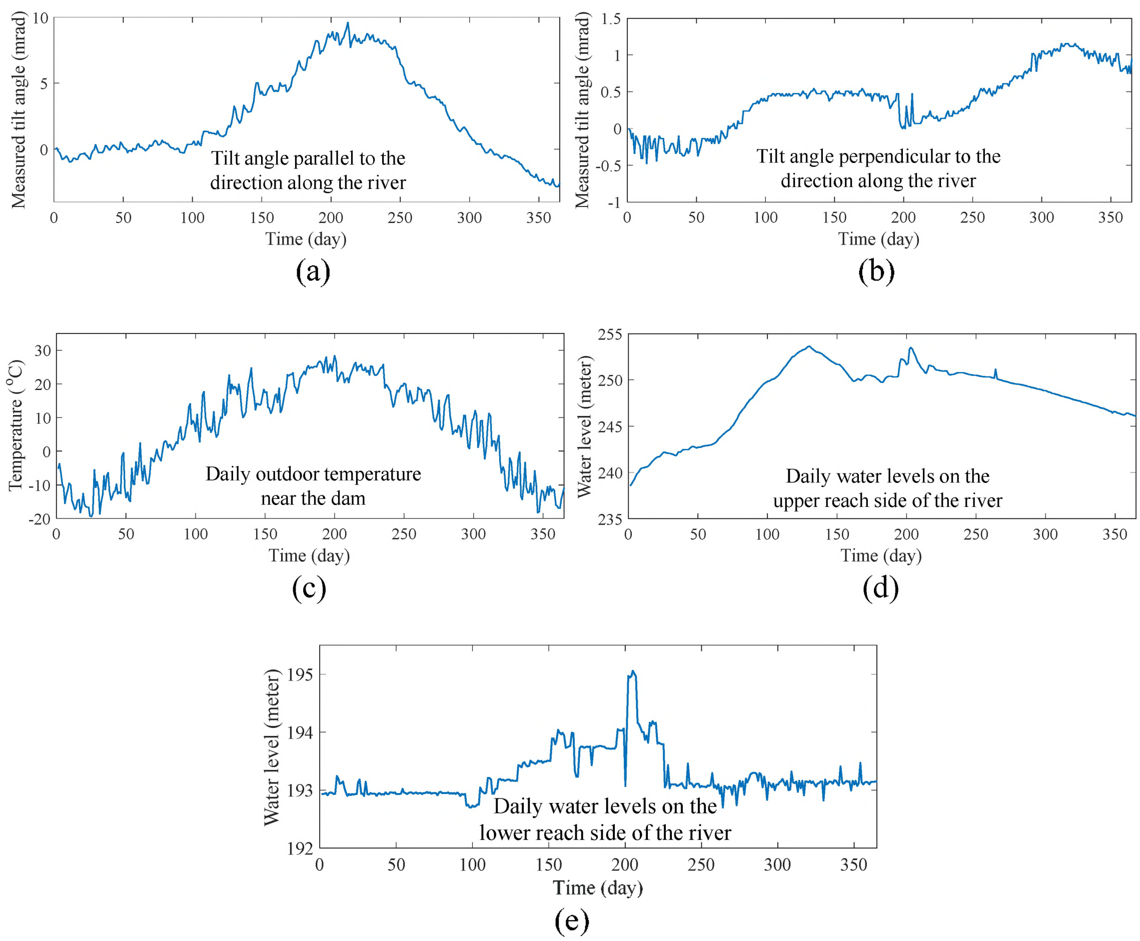

Figure 11. Plots of the daily changes in the orthogonal tilt angles of the gravity dam structure along the river and along the gravity dam compared with plots of the daily temperatures and water levels on both sides of the dam for a one-year period. (a) The daily changes in the tilt angles measured by $EFPI_2$, corresponding to tilt angles along the river. (b) The daily changes in the tilt angles measured by $EFPI_1$, corresponding to tilt angles perpendicular to the direction of the river. (c) The average daily outdoor temperatures at the Fengman Dam. (d) The daily water levels on the upper reach side of the river. (e) The daily water levels on the lower reach side of the river.

dam experiences larger thermal expansions, which makes the dam tilt towards the upper reach of the river. On the contrary, when the environmental temperature decreases, the dam tends to tilt towards the lower reach of the river. Meanwhile, the plot of the water levels of the upper reach of the river, shown in Figure 11(d), also follows a similar trend. Interestingly, the water level of the upper reach of the river was expected to have a negative correlation to the changes in the measured tilt angles of the gravity dam along the river according to the orientation of the mounted 2-D inclinometer. Our intuitive expectation is that when the water level of the upper reach of the river increases, the river water would apply a greater force to the upper reach side of the gravity dam, which would result in positive changes in the tilt angles of the top of the gravity dam towards the lower reach of the river. Surprisingly, our results indicate that the outdoor temperature changes at the gravity dam dominate the changes in the tilt angles of the gravity dam along the river. Figure 11(e) shows the water level of the lower reach of the river. Compared with the maximum change in the water level of the upper reach of the river (~15 m), the maximum change in the water level of the lower reach of the river (~2 m) is considerably smaller and sensitivity for measuring the changes in the tilt angles of a large structure over a long period of time. With a robust and easy-to-manufacture structure, our 2-D inclinometer shows significant potential for structural health monitoring, natural disaster monitoring, and other applications that require metering changes in tilt angle with high resolution, long duration, and robust instrumentation.

4. CONCLUSIONS

In this paper, we reported and demonstrated a high resolution EFPI-based 2-D optical fiber inclinometer for measuring changes in tilt angles. The 2-D inclinometer consists of a pair of perpendicularly-arranged EFPI sensors packaged inside a rectangular container box. To reduce the oscillatory effects caused by mechanical vibrations, the rectangular metal prism was connected to a cross paddle, which was immersed in a damping fluid. According to the Fabry-Perot principle, the changes in the cavity lengths of the two EFPI sensors can be calculated, and the tilt angles in the two directions of the 2-D inclinometer can be determined. The sensor design and the measurement principle were discussed. The sensitivity and measurement range of the inclinometer can be adjusted to satisfy the requirement for different practical applications. The test experiments for the two EFPI sensors, based on measuring the changes in the tilt angles of a simply-supported beam caused by a series of small loads, were presented to verify the resolution and accuracy of the prototype 2-D inclinometer. Our 2-D inclinometer shows capabilities for high-resolution measurements (~20 nrad), which exceed the resolution specifications of all optical fiber inclinometers reported to date. The 2-D inclinometer was also employed for monitoring the changes in the tilt angles of a gravity dam during a one-year period, demonstrating excellent stability and practicability. With a robust and easy-to-manufacture design, our 2-D inclinometer can be commercialized, and it shows great potential for structural health monitoring, natural disaster monitoring, and other monitoring applications conducted in harsh environments.

REFERENCES

[1] Y.-T. Ho, A.-B. Huang, and J.-T. Lee, "Development of a fibre Bragg grating sensored ground movement monitoring system," Meas. Sci. Technol., vol. 17, p. 1733, 2006.

[2] H.-F. Pei, J.-H. Yin, H.-H. Zhu, C.-Y. Hong, W. Jin, and D.-S. Xu, "Monitoring of lateral displacements of a slope using a series of special fibre Bragg grating-based in-place inclinometers," Meas. Sci. Technol., vol. 23, p. 025007, 2012.

[3] S. Vurpillot, G. Krueger, D. Benouaich, D. Clément, and D. Inaudi, "Vertical deflection of a pre-stressed concrete bridge obtained using deformation sensors and inclinometer measurements," Structural Journal, vol. 95, pp. 518-526, 1998.

[4] D. W. Ha, H. S. Park, S. W. Choi, and Y. Kim, "A wireless MEMS-based inclinometer sensor node for structural health monitoring," Sensors, vol. 13, pp. 16090-16104, 2013.

[5] Y.-G. Lee, H.-K. Jang, D.-H. Kim, and C.-G. Kim, "Development of a mirror mounted fiber optic inclinometer," Sensor. Actuat. A-Phys., vol. 184, pp. 46-52, 2012.

[6] H.-N. Li, D.-S. Li, and G.-B. Song, "Recent applications of fiber optic sensors to health monitoring in civil engineering," Engineering structures, vol. 26, pp. 1647-1657, 2004.

[7] L. Amaral, O. Frazão, J. Santos, and A. L. Ribeiro, "Fiber-optic inclinometer based on taper Michelson interferometer," IEEE Sens. J., vol. 11, pp. 1811-1814, 2011.

[8] O. Frazão, R. Falate, J. Fabris, J. Santos, L. Ferreira, and F. Araújo, "Optical inclinometer based on a single long-period fiber grating combined with a fused taper," Opt. Lett., vol. 31, pp. 2960-2962, 2006.

[9] C.-L. Lee, W.-C. Shih, J.-M. Hsu, and J.-S. Horng, "Asymmetrical dual tapered fiber Mach-Zehnder interferometer for fiber-optic directional tilt sensor," Opt. Express, vol. 22, pp. 24646-24654, 2014.

[10] P. Lu, L. Men, K. Sooley, and Q. Chen, "Tapered fiber Mach–Zehnder interferometer for simultaneous measurement of refractive index and temperature," Appl. Phys. Lett., vol. 94, p. 131110, 2009.

[11] T. Osuch, K. Markowski, A. Manujło, and K. Jędrzejewski, "Coupling independent fiber optic tilt and temperature sensor based on chirped tapered fiber Bragg grating in double-pass configuration," Sensor. Actuat. A-Phys., vol. 252, pp. 76-81, 2016.

[12] H. Bao, X. Dong, H. Gong, C. C. Chan and P. Shum, "Temperature-insensitive FBG tilt sensor with a large measurement range," 2009 Asia Communications and Photonics Conference and Exhibition (ACP), Shanghai, 2009, pp. 1-5.

[13] B.-J. Peng, Y. Zhao, Y. Zhao, and J. Yang, "Tilt sensor with FBG technology and matched FBG demodulating method," IEEE Sens. J., vol. 6, pp. 63-66, 2006.

[14] H. Y. Au, S. K. Khijwania, H. Y. Fu, W. H. Chung, and H. Y. Tam, "Temperature-Insensitive Fiber Bragg Grating Based Tilt Sensor With Large Dynamic Range," J. Lightwave Technol., vol. 29, pp. 1714-1720, 2011.

[15] H. Bao, X. Dong, L. Y. Shao, C. L. Zhao, C. C. Chan, and P. Shum, "Temperature-Insensitive 2-D Pendulum Clinometer Using Two Fiber Bragg Gratings," IEEE Photonic. Tech. L, vol. 22, pp. 863-865, 2010.

[16] X. Dong, H. Tam, and P. Shum, "Temperature-insensitive strain sensor with polarization-maintaining photonic crystal fiber based Sagnac interferometer," Appl. Phys. Lett., vol. 90, p. 151113, 2007.

[17] S. Liu, N. Liu, M. Hou, J. Guo, Z. Li, and P. Lu, "Direction-independent fiber inclinometer based on simplified hollow core photonic crystal fiber," Opt. Lett., vol. 38, pp. 449-451, 2013.

[18] Q. Rong, X. Qiao, T. Guo, H. Yang, Y. Du, D. Su, et al., "Orientation-dependant inclinometer based on intermodal coupling of two-LP-modes in a polarization-maintaining photonic crystal fiber," Opt. Express, vol. 21, pp. 17576-17585, 2013.

[19] D.-H. Kim, "A fiber-optic tiltmeter system based on the moiré-fringe effect," Meas. Sci. Technol., vol. 20, p. 025203, 2008.

[20] H.-Y. Chang, Y.-C. Chang, and W.-F. Liu, "A highly sensitive two-dimensional inclinometer based on two etched chirped-fiber-grating arrays," Sensors, vol. 17, p. 2922, 2017.

[21] Z. Chen, G. Hefferman, L. Yuan, Y. Song, and T. Wei, "Terahertz-range interrogated grating-based two-axis optical fiber inclinometer," Optical Engineering, vol. 55, p. 026106, 2016.

[22] B. P. Abbott, R. Abbott, T. Abbott, M. Abernathy, F. Acernese, K. Ackley, et al., "Observation of gravitational waves from a binary black hole merger," Phys. Rev. Lett., vol. 116, p. 061102, 2016.

[23] Y. Huang, T. Wei, Z. Zhou, Y. Zhang, G. Chen, and H. Xiao, "An extrinsic Fabry–Perot interferometer-based large strain sensor with high resolution," Meas. Sci. Technol., vol. 21, p. 105308, 2010.

[24] Y.-J. Rao, "Recent progress in fiber-optic extrinsic Fabry–Perot interferometric sensors," Opt. Fiber Technol., vol. 12, pp. 227-237, 2006.

[25] M. Schmidt, B. Werther, N. Fürstenau, M. Matthias, and T. Melz, "Fiber-Optic Extrinsic Fabry-Perot Interferometer Strain Sensor with< 50 pm displacement resolution using three-wavelength digital phase demodulation," Opt. Express, vol. 8, pp. 475-480, 2001.

[26] C. Zhu, Y. Chen, Y. Zhuang, Y. Du, R. E. Gerald, Y. Tang, et al., "An optical interferometric triaxial displacement sensor for structural health monitoring: characterization of sliding and debonding for a delamination process," Sensors, vol. 17, p. 2696, 2017.

[27] Y. Du, Y. Chen, Y. Zhuang, C. Zhu, F. Tang, and J. Huang, "Probing Nanostrain via a Mechanically Designed Optical Fiber Interferometer," IEEE Photonic. Tech. L, vol. 29, pp. 1348-1351, 2017.

[28] Y. Du, Y. Chen, C. Zhu, Y. Zhuang, and J. Huang, "An embeddable optical strain gauge based on a buckled beam," Rev. Sci. Instrum., vol. 88, p. 115002, 2017.

[29] Y. Zhuang, Y. Chen, C. Zhu, R. E. Gerald, and J. Huang, "Probing changes in tilt angle with 20 nanoradian resolution using an extrinsic Fabry-Perot interferometer-based optical fiber inclinometer," Opt. Express, vol. 26, pp. 2546-2558, 2018.

[30] Y. Yang, E. Wang, K. Chen, Z. Yu, and Q. Yu, "Fiber-Optic Fabry–Perot Sensor for Simultaneous Measurement of Tilt Angle and Vibration Acceleration," IEEE Sens. J., vol. 19, pp. 2162-2169, 2018.

[31] R. W. Hertzberg, R. P. Vinci, and J. L. Hertzberg, Deformation and fracture mechanics of engineering materials vol. 89: Wiley New York, 1996.

[32] C. Zhu, Y. Chen, Y. Du, Y. Zhuang, F. Liu, R. E. Gerald, et al., "A displacement sensor with centimeter dynamic range and submicrometer resolution based on an optical interferometer," IEEE Sens. J., vol. 17, pp. 5523-5528, 2017.

III. FIBER OPTIC SENSOR EMBEDDED SMART HELMET FOR REAL-TIME IMPACT SENSING AND ANALYSIS THROUGH MACHINE LEARNING

Yiyang Zhuang[a], Qingbo Yang[a], Taihao Han[b], Ryan O'Malley[a], Aditya Kumar[b], Rex E. Gerald II[a*], and Jie Huang[a*]

[a]Department of Electrical and Computer Engineering, Missouri University of Science and Technology, Rolla, MO 65409, U.S.A.
[b]Department of Materials Science and Engineering, Missouri University of Science and Technology, Rolla, MO 65409, U.S.A.

*Corresponding authors
Jie Huang (jieh@mst.edu)
Rex E. Gerald II (geraldr@mst.edu)

ABSTRACT

Background: Mild traumatic brain injury (mTBI) strongly associates with chronic neurodegenerative impairments such as post-traumatic stress disorder (PTSD) and mild cognitive impairment. Early detection of concussive events would significantly enhance the understanding of head injuries and provide better guidance for urgent diagnoses and the best clinical practices for achieving full recovery.

New method: A smart helmet was developed with a single embedded fiber Bragg grating (FBG) sensor for realtime sensing of blunt-force impact events to helmets. The transient signals provide both magnitude and directional information about the impact event, and the data can be used for training machine learning (ML) models.

Results: The FBG-embedded smart helmet prototype successfully achieved real-time sensing of concussive events. Transient data "fingerprints" consisting of both magnitude and direction of impact, were found to correlate with types of blunt-force

impactors. Trained ML models were able to accurately predict (R^2 ~ 0.90) the magnitudes and directions of blunt-force impact events from data not used for model training.

Comparison with existing methods: The combination of the smart helmet data with analyses using ML models provides accurate predictions of the types of impactors that caused the events, as well as the magnitudes and the directions of the impact forces, which are unavailable using existing devices.

Conclusion: This work resulted in an ML-assisted, FBG-embedded smart helmet for real-time identification ofconcussive events using a highly accurate multi-metric strategy. The use of ML-FBG smart helmet systems canserve as an early-stage intervention strategy during and immediately following a concussive event.

Keywords: Mild traumatic brain injury; Fiber-optic sensor; Fiber Bragg grating; Machine learning; Concussive events; Blunt-force impact-induced brain injury

1. INTRODUCTION

Post-traumatic stress disorder (PTSD), physical health problems, mild cognitive impairment, dementia, and depression are strongly associated with mild traumatic brain injury (mTBI), as frequently re- ported in military-, sport-, and other source-induced head injuries (Faul et al., 2010; Guskiewicz et al., 2007; Hoge et al., 2008). Although post-traumatic brain injury assessments and interventions have been discussed and practiced for decades, the importance of immediate detection and early diagnosis cannot be over-emphasized (Brenner et al., 2009). Unfortunately, the lack of practical early detection tools weakens the predictive measures for mTBIs.

Early detection of blunt-force impact events by advanced commercially-available hardware, such as the Reebok Checklight skullcap module (Harper et al., 2018), relies heavily on the devices'portability and robustness to ensure high fidelity capture of concussion-causing events in vivo. Another reason to use sensor-integrated wearable devices for early-stage intervention during blunt-force impact events is that wearable devices can, apparently, serve as dynamic platforms for instantaneous sensing. In particular, for pro- tective head equipment, a helmet's original purpose was to redistribute and limit the forces directed at the head to levels that are below the skull fracture tolerances. Advanced helmets were designed to increase the duration of strikes to the head and thereby limit peak head acceleration, which ultimately protects the underlying bone and neurovascular structures (Butz and Dennison, 2015). In the present work, the direct embedment of a fiber-optic sensor in a thin surface layer of the shell of a helmet could further expand the helmet's functionality in two important aspects: (1) Sensing and analyzing blunt-force impact events could provide direct avenues for evaluating the capabilities of helmets for head protection, which may inspire better ways to design and construct helmets; and (2) Evaluating the potential physiological effects of blunt-force impact events in real-time using ML models will identify a range of concussive events that should be treated within the Golden Hour, leading to best practices and positive long-term health outcomes. Fiber-optic sensors – as thin as human hairs – have been employed in wearable sensing devices without compromising the devices' protective structure and functionality (Grattan and Sun, 2000; Lee, 2003; Rao, 2006). The fiber Bragg grating (FBG) sensing principle has been widely adopted for monitoring impact-induced strain changes (Guan et al., 2000; Ho et al., 2006). By creating periodic variations in the refractive index along the length of the core of the optical fiber, subtle wavelength changes due to variations in strain can be pinpointed. This simple sensing method enables signal demodulation that is facile and rapid (~kHz sampling rates), hence making it possible to sense high-speed mechanical events in real-time. Butz et al. fabricated the first-of-its-kind force transducer based on the FBG principle and successfully integrated the device into a helmet for measuring transient forces that resulted from impacts to a dummy head (Butz and Dennison, 2015). A single FBG fiber was immobilized on a fixed-fixed beam of an aluminum superstructure that was embedded into the contoured surface of a helmet. Under computer-programmed externally-applied impacts, the deformation of the fixed-fixed beam resulted in the changes in the strain of the FBG section of the embedded fiber. The magnitudes of the strain changes were found to be proportional to the applied impact forces. The requirements of ample space on the surface of the helmet shell for multiple FBG transducers embedment severely limited the feasibility of this method when sensing at a multitude of points is needed across the surface of the helmet. Such limitations on the number of embeddable sensors in the helmet shell will inevitably limit the quantity of the data retrieved from the blunt-force impact events, in turn limiting the overall efficacy of mTBI detection, and subsequent capabilities for mitigation of adverse long-term physiological effects.

The present study focused on the application of single fiber FBGs, without mechanical superstructures (Butz and Dennison, 2015), to maximize their advantages in terms of unconstrained degrees of freedom, small size, and light weight for wearable and robust sensing under dynamic conditions. Moreover, the study exploited the combination of FBG sensors with machine learning (ML) models to enhance analytical capabilities for multifaceted analyses of complex transient signals. The ML models have been introduced to many areas of funda- mental and applied research to extract complicated and important at- tributes from high-value data. The utilization of ML models for fiber-optic communicating, sensing, and predicting has also been re- ported previously (Jarajreh et al., 2014; Karanov et al., 2018; Makar- enko, 2016; Mazid and Ali, 2008; Tejedor et al., 2017; Wang et al., 2015). For instance, Mazid et al. applied the Support Vector Machine (SVM) model to a database from an opto-tactile sensor and successfully identified patterns of different surface textures (Mazid and Ali, 2008). Makarenko et al. demonstrated an approach to building deep learning models for a fiber-optic distributed sensing system, which could function with high degrees of adaptability under intensive signal-jamming environments (Makarenko, 2016).

Thus, the combination of a specific fiber-optic FBG sensing principle with carefully selected and rigorously trained ML models may fulfill the studies stated goals due to the following reasons: (1) The combined utilization of fiber-optic sensing data with ML models will avoid the tedious modeling and calibration approaches that are required by traditional data-handling tools, such as finite element analysis (FEA); (2) ML analysis can substantially enhance pattern recognition abilities, thereby helping to reveal and identify hidden linkages between transient signals from fiber-optic sensors and various impact parameters, such as the impact sources, magnitudes, directions, and so forth, that are monitored and recorded; and (3) Well-trained and fully-validated ML models may thus provide accurate predictions for the blunt-force impact events such that mitigating actions can be taken within that first hour after the occurrence of an injury – or the Golden Hour – which can go a long way in protecting the long-term mental health of the individual.

Presented in this study are an FBG sensor-embedded smart helmet, ML-models for sensing, and subsequent multifaceted analyses of tran- sient concussive events. A bowling ball Pendulum Impactor System (PIS) was constructed and employed for simulating concussive events on a dummy head equipped with the fiber-optic sensor-embedded smart helmet. Multiple impact kinetic energy levels and directions were tested to validate the system's robustness for sensing blunt-force impact events. A LabVIEW program was coded to autonomously output a real- time display of the Bragg wavelength shifts caused by changes in strains of the FBG sensor. The resultant datasets were utilized for training several ML models, and to subsequently conduct performance tests. Finally, the prediction accuracies of these ML models were compared and discussed.

2. MATERIALS AND METHODS

2.1. FBG SENSING PRINCIPLE AND SENSOR FABRICATION

An illuminated coil of optical fiber with an expanded view depicting the structure of a Fiber Bragg Grating (FBG)—including the external space (air), cladding, core, grating, respective indicators for refractive indices, and grating period—is shown in Figure 1. The FBG is formed by creating a periodic variation in the refractive index along the core of the optical fiber. The periodic pattern functions as a notch filter. It reflects the incident light at a particular wavelength and transmits light of all other wavelengths. The periodic pattern can be created using various methods, such as interference lithography, phase mask writing, and point-by-point writing. The wavelength of the reflected light (λ_B), which is called the Bragg wavelength, is defined as follows:

$$\lambda_B = 2n_{eff}\Lambda \tag{16}$$

where n_{eff} is the effective refractive index of the core of the optical fiber and Λ is the grating period. When an FBG sensor is subjected to an applied strain or a temperature

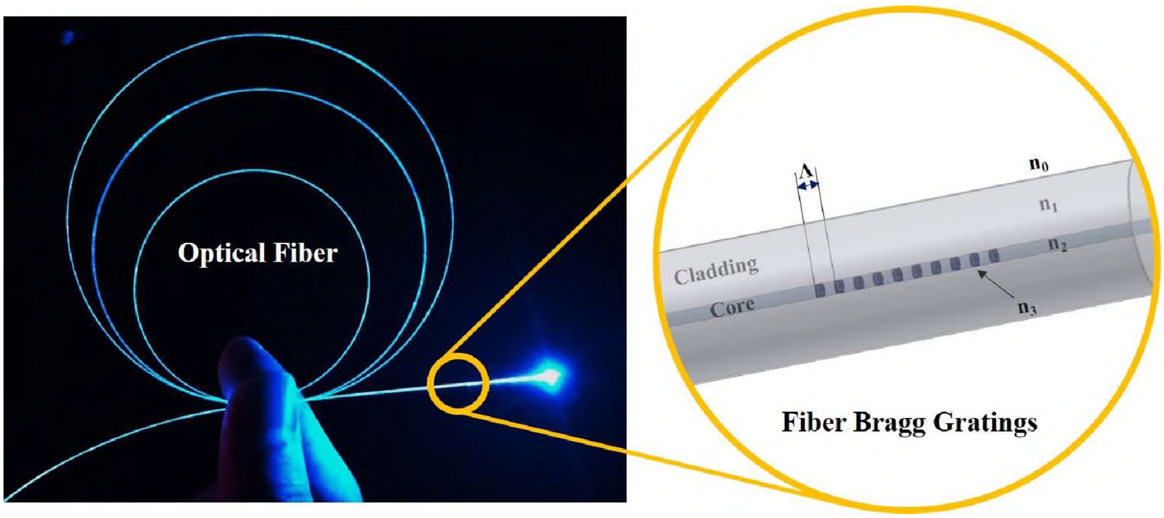

Figure 1. A coil of optical fiber with an expanded view depicting the fiber Bragg grating (FBG) structure in the core of a single-mode optical fiber. The labels, n_0, n_1, n_2 and n_3 represent the refractive index of the air, fiber cladding, fiber core and the fabricated grating, respectively. Λ represents the grating period. The optical fiber also serves the dual purpose of a low-loss conduit for transferring the information from the FBG sensor to a remote location where the interrogator is located.

change, the refractive index of the fiber core and the grating period will experience variations, resulting in shifts of the Bragg wavelength. Assuming the applied strain or temperature change is uniform, the Bragg wavelength shift $\Delta\lambda_B$ is described as:

$$\frac{\Delta\lambda_B}{\lambda_B} = (1 - p_e)\Delta\varepsilon + (a_{cte} + a_{cto})\Delta T \tag{2}$$

where p_e, $\Delta\varepsilon$, a_{cte}, a_{cto}, and ΔT are the strain-optic coefficient, the strain variation, the thermal expansion coefficient, the thermo-optic coefficient, and the change in temperature, respectively. Therefore, by continuously monitoring the wavelength of the reflected light, the shift of the Bragg wavelength can be determined, and the applied strain or temperature change can be calculated. Although both strain and temperature perturbations will simultaneously influence FBG wavelength shifts, the timescales of changes in strain induced by blunt-force impact events typically range from one to tens of milliseconds (ms), which are much shorter than the timescales of FBG signal fluctuations induced by variations in temperature. Therefore, the temperature factors can be neglected from the Eq. (2) [56]. The shift in wavelength of the FBG caused by an axial strain on an SMF-28 fiber can be written as:

$$\frac{\Delta\lambda_B}{\lambda_B} = 0.79\Delta\varepsilon \tag{3}$$

2.2. INTEGRATION OF AN FBG SENSOR IN A HELMET

Figure 2 shows a photograph of a prototype smart helmet used in this study with an embedded FBG sensor and a schematic diagram of the interrogation system. The FBG sensors were fabricated from a single-mode optical fiber (SMF-28) employing a *femto*second fabrication system (Newport *femto*FBG) and were embedded inside shallow grooves on the top surfaces of football helmets (Schutt kids' AiR standard VI football helmet) as shown in Figure 2a. The groove was made on the outer surface of the helmet using a momentary-contact wire heater, which resulted in a groove depth of 1 mm and a groove length of 25 mm. An optical fiber (length, ~ 1 m) with an FBG sensor (length, ~ 1 cm) was placed inside the groove (red arrow), and the groove was filled with epoxy. After the epoxy solidified, the free end of the optical fiber on the backside of the helmet was spliced to an extension optical fiber and connected to the interrogation system. It should be

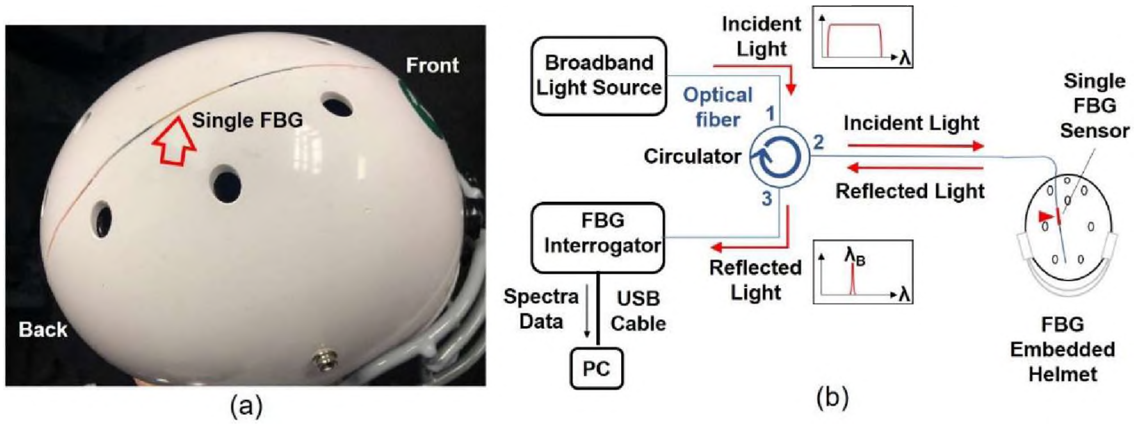

Figure 2. The first prototype Missouri S&T smart helmet equipped with an FBG sensor embedded in a shallow groove on the top surface. (a) A photograph of the upper side of the helmet where the FBG fiber was embedded (red arrow). (b) A schematic diagram of the interrogation system for the smart helmet.

noted that in a preliminary approach, FBG sensors were embedded into shallow grooves created by applying a heated wire on the outer surfaces of the helmets. Due to the small size of SMFs, the fibers, including the FBG sensor section, could be embedded into the helmets during the manufacturing process so that the smart helmet can function without a compromised mechanical integrity of the plastic shell. When a blunt-force impact is applied to the helmet, a transient material deformation around the impact spot will generate momentary stresses. Based on the directions of force propagations, such stresses will stretch and compress the embedded FBG sensor along the axial direction, cause variations of strain to the fiber, and finally induce a transient shift of the FBG wavelength that can be determined by Eq. (3).

2.3. DATA COLLECTION AND INTERROGATION

A schematic diagram of the interrogation system for the FBG-equipped smart helmet is illustrated in Figure 2(b). The incident light from the broadband light source

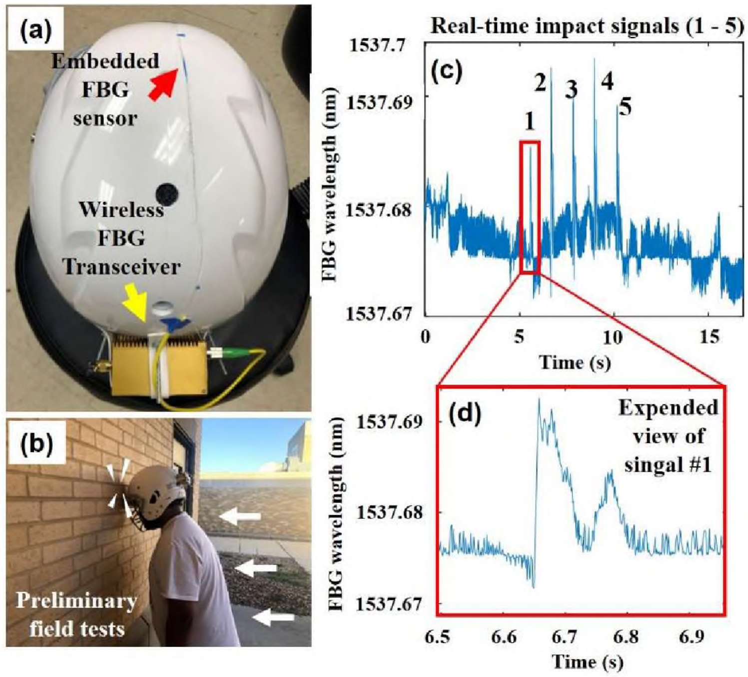

Figure 3. Testing a prototype wireless smart helmet for recording blunt-force impact events in the field. (a) A top view of the smart helmet with the wireless Redondo FBG transceiver mounted to the rear of the helmet. Both the FBG sensor location (red arrow) and the wireless FBG Transceiver module (yellow arrow) are indicated in the photograph. The fiber-optic FBG sensor is connected to the Redondo module via the yellow-green connector. (b) Photograph of the wall-impact scene, where a student tester is wearing the helmet and impacting the wall at a mild level. (c) Signals that were immediately transmitted from the Redondo module to a remote laptop located at a distance of 10 meters. The plot in (c) shows five consecutive events generated by five corresponding impacts of the helmet on a brick wall. (d) The expanded view of the first event in (c) shows two peaks, the first from the initial contact and the second from the rebound contact.

(Thorlabs ASE-FL7002-C4 ASE Source) was directed into the FBG fiber sensor through an optical fiber circulator (from Port 1 to Port 2). Then a portion of the incident light with wavelength satisfying the Bragg wavelength (Eq. (1)) was reflected and redirected to the circulator (from Port 2 to Port 3) and detected by the interrogator (BaySpec FBGA-F-1510-1590-FA). To readily detect and reconstruct the blunt-force impact events, the acquisition speed of the interrogator was set to a sampling rate of 5 kHz, corresponding to a 0.2 ms time interval between sampled signals. The recorded signals were then uploaded to the computer for further processing.

2.4. IMPLEMENTATION OF A WIRELESS DATA TRANSMISSION MODULE

Figure 3 shows a prototype smart helmet configured with a wireless FBG transceiver for field tests. The wireless FBG transceiver (Redondo Optics MOFIS FBG Transceiver) was employed to enable detection and interrogation of blunt-force impact events and the wireless transmission of the collected and processed FBG data. The Redondo device is a miniaturized transceiver with a built-in light source, a wireless communication module, and an on-board power source. It can monitor signals from two FBG sensors fabricated in one single fiber with a high sampling rate (up to 20 kHz). To prepare the smart helmet, a groove with 0.5 mm depth was heat-carved into the top surface of the football helmet. One FBG sensor was placed inside the groove and fixed in place using epoxy. The Redondo FBG transceiver was mounted on the rear of the football helmet and connected to the embedded FBG sensor. The final layout of the smart helmet is shown in Figure 3 (a).

The functionality of the smart helmet was tested outside the lab building to simulate a basic field test condition. During the test, a student tester impacted a brick wall while wearing the helmet at force levels that were mild enough to avoid any head injuries, as illustrated in the photograph in Figure 3 (b). The helmet was equipped with full internal cushion protection and no initial external force was applied to the tester's body to ensure that he had full control over the force being used to impact the brick wall. The signals recorded from the embedded FBG sensor were transmitted in real-time to a nearby laptop via Redondo. The distance between the student tester and the laptop was 10 meters. An example of FBG sensor data from five rapid, consecutive impacts (with a total test sequence duration of fewer than 20 seconds) is shown in Figure 3 (c). The expanded view of the first impact event in the sequence, shown in Figure 3 (d), reveals a double-peak signal output by the FBG sensor over approximately 0.2 seconds.

2.5. SIMULATION OF BLUNT-FORCE IMPACT EVENTS USING A PENDULUM IMPACTOR SYSTEM

To demonstrate the functionality of the FBG-embedded smart helmet, a home-built bowling ball Pendulum Impactor System (PIS) was utilized to simulate blunt-force impact events on a dummy head wearing a smart helmet prototype. A photograph of the system is shown in Figure 4 (a). A manikin was placed in the center of a metal support frame. A bowling ball was suspended from the frame using ¼-in weldless silver steel cable, such that it was barely contacting the test helmet while at rest. The goal of this setup is to emulate a perfectly elastic collision, meaning all the potential energy of the bowling ball release height is imparted to the manikin/helmet prototype upon impact. This setup provides a good approximation of the kinetic energy of the impact event, but it does ignore energy lost to sound, and helmet deformation. The test included impacts of five magnitudes, simulated by adjusting the initial height from which the bowling ball was released (0.04 m, 0.14 m, 0.24 m, 0.34 m and 0.44 m). The five impacts were administered to the helmet at four angles: 0°, 90°, 180°, and 270° (Figure 4 (b)). The procedure was repeated a total of three times. By assuming the impact is elastic, the amount of kinetic energy for each impact is equal to the potential energy. The weight of the bowling ball was 4.9 kg. The potential energies of the impacts correspond to the release heights of the bowling ball. The impact

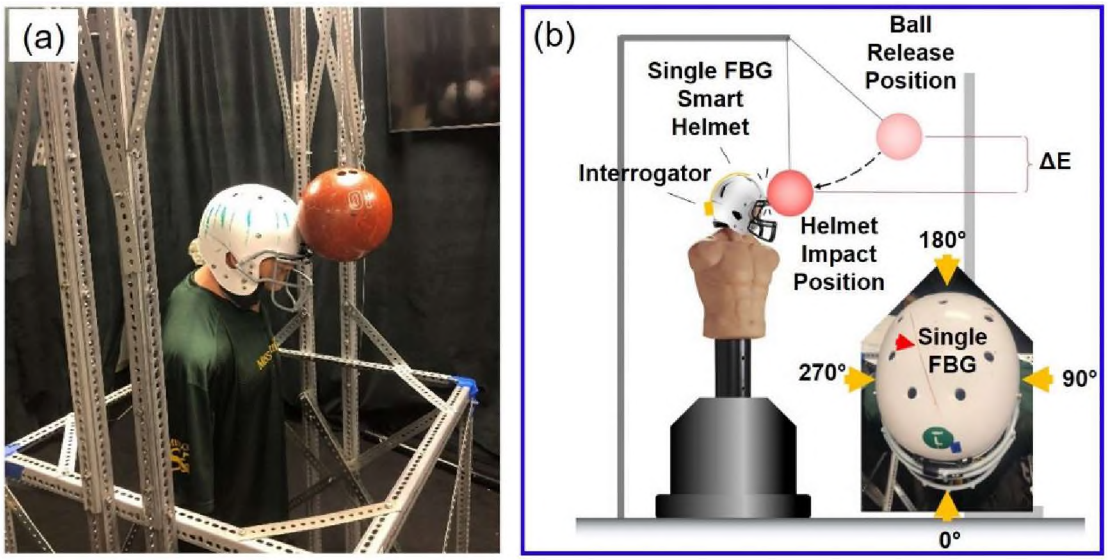

Figure 4. A Pendulum Impactor System (PIS) that employs a bowling ball to simulate blunt-force impact events. (a) A photograph of the PIS consisting of a rigid metal frame and a separate steady base to hold the manikin and helmet in place. A bowling ball is suspended in front of the dummy head and released from a designated height to cause the impact. (b) A schematic diagram illustrating how the PIS functions. The suspended bowling ball is released from a designated height and impacts the FBG-embedded helmet at the lowest position of its arc trajectory. The top view of the helmet shown in the photograph in (b) illustrates the four angles of impact used in the test: 0°, 90°, 180°, and 270°.

energies used in the investigation were 1.80 J, 6.31 J, 10.82 J, 15.33 J, and 19.84 J for the list of heights mentioned previously. The helmet was positioned such that the bowling ball made contact with the helmet at the lowest point in its trajectory so that the calculated potential energy was completely converted to kinetic energy upon impact. In most tests, the kinetic energy was efficiently transferred to the helmet. However, it is known that this is not a perfectly elastic collision, and in some cases the bowling ball was observed bouncing back slightly with low speed, indicating the true inelastic nature of the impact setup. This is most likely due to helmet deformation or manikin natural frequency response to the impact energy. Given these known losses the calculated potential energy is assumed to provide a good approximation of the initial source energy. Both impact heights and directions were recorded for all impact events.

2.6. MACHINE LEARNING (ML) MODEL SELECTION

To avoid tedious and complicated unsupervised statistical modeling when dealing with the raw transient signal datasets, the strong pattern recognition ability of machine learning (ML) was utilized. Five standalone ML models and two ensemble ML models were used in this study: Support Vector Machine (SVM), Gaussian Process Regression (GPR), Random Forest (RF), K-Nearest Neighbor Instance-Based Learner (IBK), Elastic Net Regression (ENR), Voting, and Additive Regression-Random Forest (AR-RF). These seven ML models are commonly used for similar types of datasets and tend to produce more accurate predictions compared to other ML models [57-59].

2.7. ML MODEL TRAINING AND PREDICTION

To determine which ML model performed best with the FBG sensor-embedded helmet, each of the selected models was trained and their prediction performances were benchmarked against new (raw) transient signals. The aforesaid assessment of prediction performance is based on the model's prediction accuracy, where 75% of the raw signals with known impact heights and directions were used to train the models, then the remaining 25% of the raw signals were treated as unknown domain for models to make predictions about impact height and direction. The more untrained raw signal data-records that fall into the model predicted area, the better the performance of the selected ML model, as indicated by a lower data-prediction deviation and a higher coefficient of determination (R^2). The

75%-25% data split ratio has widely been adopted in ML model training and has shown good performance results [57-62]. Here, a random data selection is crucial to ensure that the training data is representative of the original (parent) set and to guarantee that the input values are inclusive through the entire range.

3. RESULTS

3.1. DISTINGUISH TYPES OF IMPLEMENTS USED TO SIMULATE THE BLUNT-FORCE IMPACT EVENTS

A series of preliminary impact events were carried out using different impactors to validate the functionality of the FBG-embedded smart helmet and interrogation system. The impactors included an Allen wrench, a hammer, and a padded PVC pipe (simulating a “pugil stick” used in military training), which were chosen to cause distinguishable blunt-force impact events to the smart helmet prototype. Here, the immediate signal received from the interrogator was displayed as the magnitude of a blunt-force impact metric versus time. Distinctive peak-and-valley patterns were observed along the time axis, as demonstrated in Figure 5. The blunt-force impact by an Allen wrench resulted in an initial sharp and rapid signal oscillation, followed by a similar oscillatory pattern with reduced intensity. The blunt-force impact caused by the hammer resulted in a sharp, but broader peak when compared to the impact of the Allen wrench. Interestingly, the blunt-force impact caused by the simulated “pugil stick” resulted in an initial transient oscillatory signal that was somewhat similar to that of the Allen wrench, but extended to multiple periodic signal peaks with gradually broadened peak shapes.

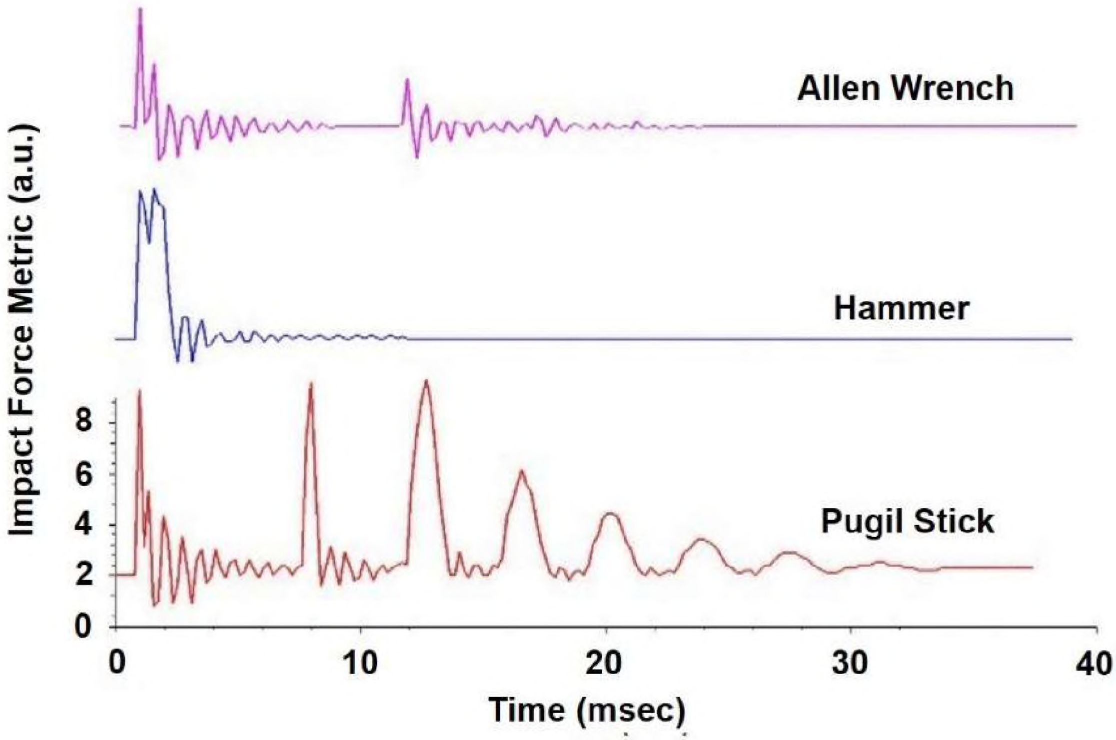

Figure 5. Plots of blunt-force impact (uniform scale, au) versus impact time (ms) showing distinguishable signal oscillation traces caused by an Allen wrench (top), a hammer (middle) and a "pugil stick" (bottom). Each blunt-force impact event resulted in a transient deformation of the smart helmet that was metered by a single FBG sensor embedded in the smart helmet.

3.2. RAW TRANSIENT SIGNAL RESULTS GENERATED BY CONTROLLED BLUNT-FORCE IMPACT EVENTS

The FBG-embedded smart helmet prototype was quantitatively evaluated using a home-built bowling ball PIS. Controlled blunt-force impact events were created by adjusting impact magnitudes (controlled by the bowling ball's release height) and directions (controlled by the bowling ball's angle of impact). Results are shown as the relative wavelength shift vs. time within the first 200 ms. Distinguishable patterns of peaks and valleys were observed as exemplified in Figure 6. Most peaks and valleys were distributed within the first 80 – 100 ms, where 5 – 10 signal features repeatedly appeared at the same or similar time points (black arrows), though their magnitudes varied due to the different levels of impact energy that were applied. Such pattern repetition is uniquely correlated with each impact direction. When impact direction changed from the front (Figure 6 (a)), left side (Figure 6 (b)) to the rear (Figure 6 (c)) and the right side (Figure 6 (d)), the peak-and-valley pattern also changed accordingly. All transient oscillatory signals recorded during the tests were used for ML model training or prediction.

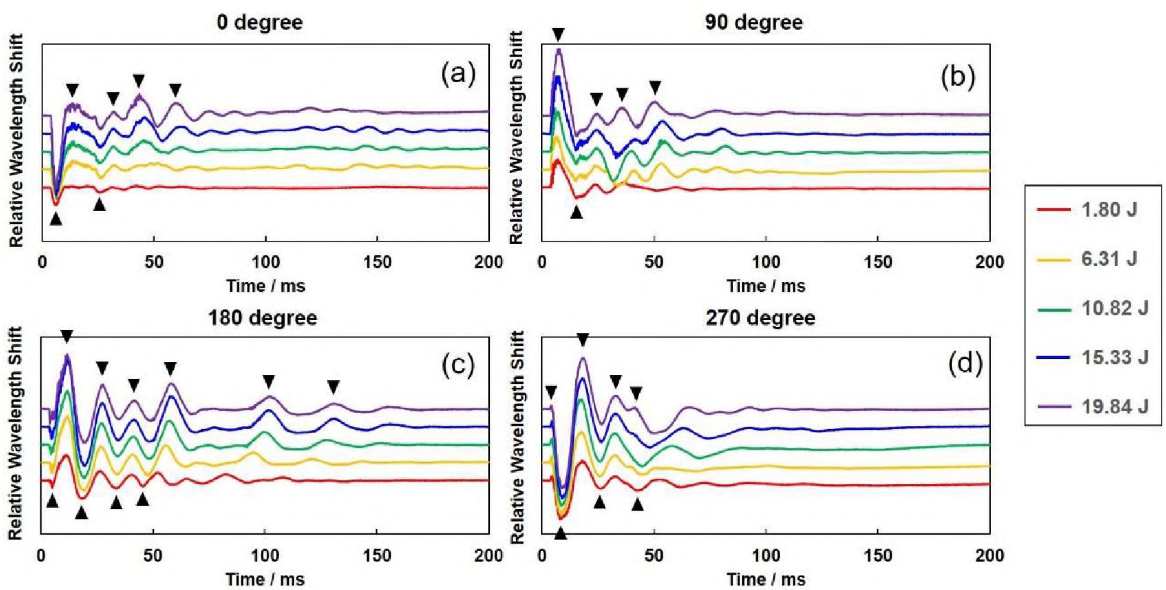

Figure 6. First 200 ms of the transient oscillatory signals resulting from impacts using the PIS at four different directions (0°, 90°, 180°, and 270°) and five different kinetic energy levels (1.80J, 6.31J, 10.82J, 15.33J, and 19.84J). The directions of the blunt-force impact include (see Figure 4 (b)): (a) Head-on, (b) left side, (c) Rear and (d) right side. Black arrows indicate typical spectral peaks and/or valleys that may potentially serve as a "fingerprint" for a specific impact direction.

3.3. RAW TRANSIENT SIGNAL RESULTS GENERATED BY CONTROLLED BLUNT-FORCE IMPACT EVENTS

Five standalone and two ensemble ML models were trained using 75% of the transient oscillatory signals collected from the basic test and evaluated using the remaining 25% of the transient oscillatory signals. The results indicate that the combined use of the FBG sensor embedded on the smart helmet and the ML models can predict the initial kinetic energy (i.e., ball release heights, Figure 7) and direction (Figure 8) of an impact. Although most ML models produced predictions with reasonable accuracies, their

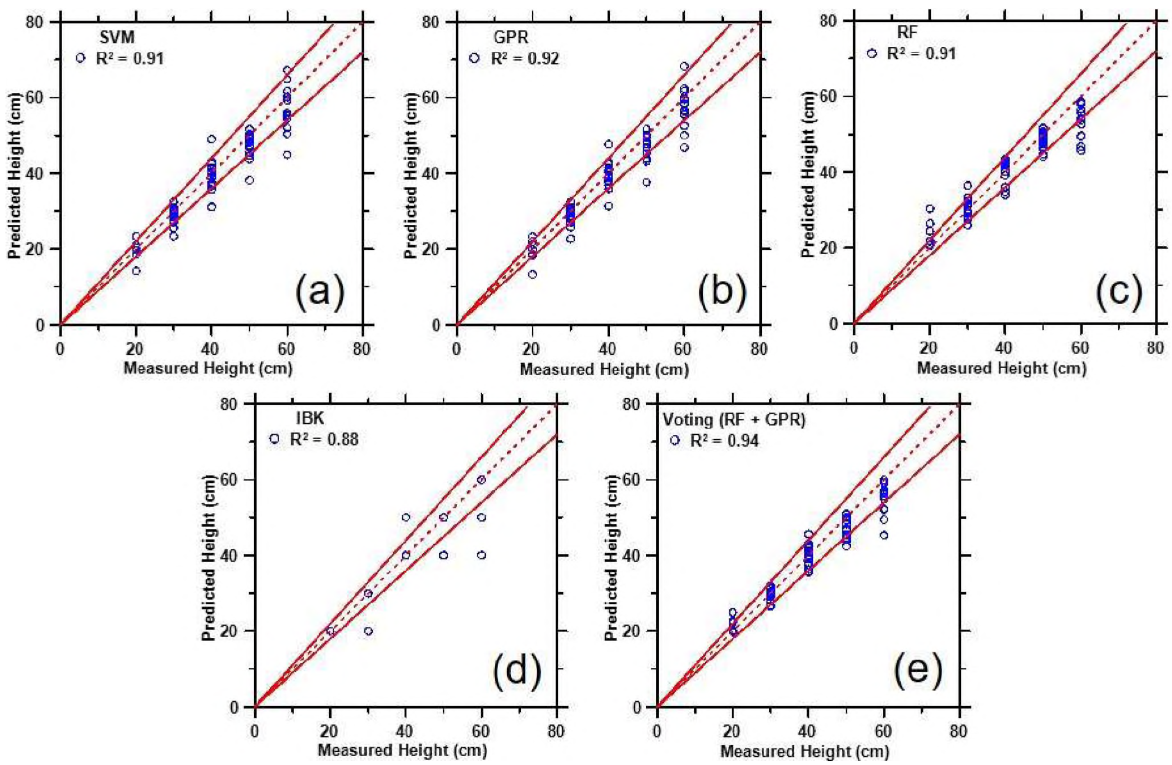

Figure 7. Graphs of Predicted Height versus Measured Height derived from several ML models. The ML models employed include: (a) Support Vector Machine (SVM), (b) Gaussian Process Regression (GPR), (c) Random Forest (RF), (d) K-Nearest Neighbor Instance-Based Learner (IBK), and (e) Voting (RF+GPR). The plotted data represent 25% of the parent database that was not previously included in the training process of the ML models. The dashed line represents the line of ideality and the solid lines represent ±10% boundaries.

prediction performances (assessed in terms of R^2 values) were slightly different from one another. Overall, based on R^2 assessments for predictions of the initial energies of the impacts, the ML models were ranked as voting > GPR > SVM > RF > IBK, with R^2 values ranging from 0.88 to 0.94. Based on R^2 for predictions of impact directions, the ML models can be ranked as AR-RF > RF > ENR > GPR > SVM, with R^2 values ranging from 0.91 to 0.99.

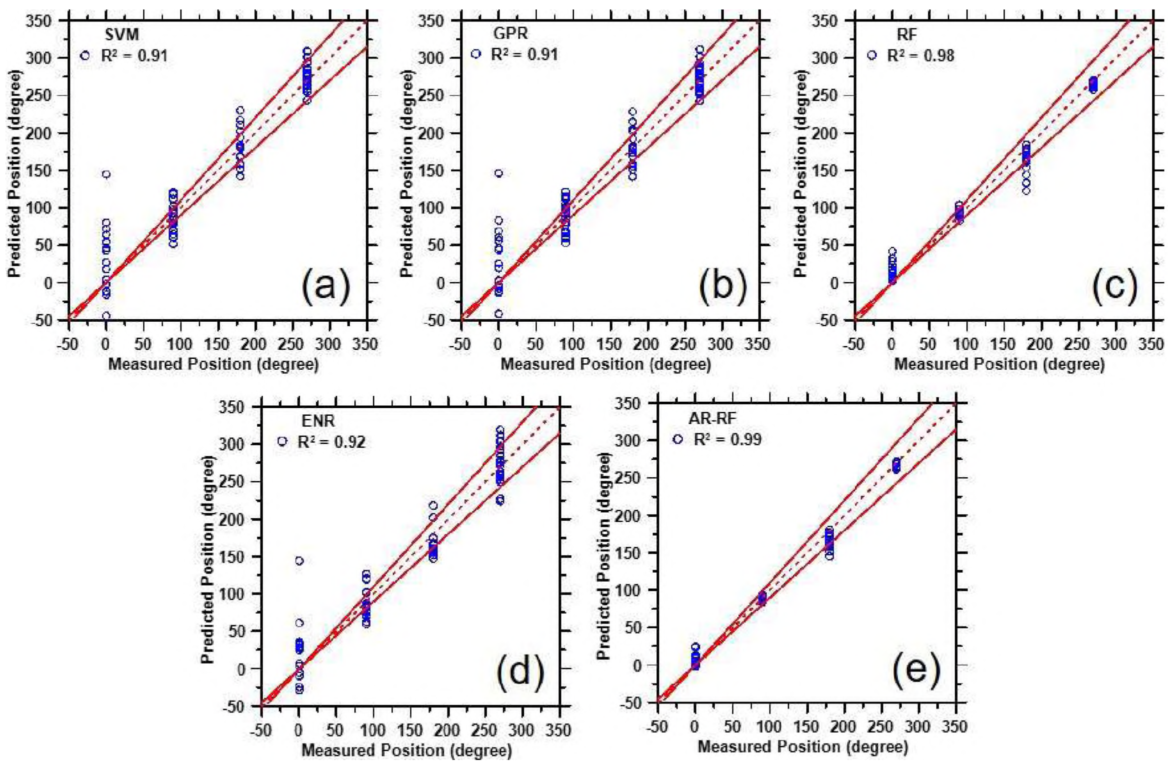

Figure 8. Graphs of predicted impact directions (positions) versus measured directions (positions) derived from several ML models. The ML models employed include: (a) Support Vector Machine (SVM), (b) Gaussian Process Regression (GPR), (c) Random Forest (RF), (d) Elastic Net Regression (ENR), and (e) Additive Regression-Random Forest (AR-RF). The plotted data represent 25% of the parent database that was not previously included in the training process of the ML models. The dashed line represents the line of ideality and the solid lines represent ±10% boundaries.

4. DISCUSSION

Researchers have been pursuing the ability to immediately sense and evaluate head injuries induced by blunt-force impacts for decades. Despite medical advancements in recent years, individuals with head injuries caused by blunt-force impacts must often wait for hours or even days to have a thorough medical check via formal protocols such as magnetic resonance imaging (MRI) or positron emission tomography (PET). Unfortunately, this delay in assessment means that injured individuals often do not have access to the best medical/clinical practices for the treatment of blunt-force impacts, which are typically prescribed within the Golden Hour. In the future, the diagnosis of head injuries induced by blunt-force impacts should rely on *in situ* sensing devices to enable immediate assessment of critical parameters that may correlate with harmful effects on the individual.

In 2009, Cheriyan et al. attempted to achieve immediate sensing and evaluation of head injuries. The researchers combined electroencephalography (EEG) electrodes, accelerometers, pressure sensors, blood-oxygen saturation (SpO2) sensors, and remote communication/control devices, integrating them into the head pad of an Advanced Combat Helmet to monitor military personnel for physiological indicators of mTBI [63]. EEG is sensitive and accurate enough for mTBI diagnosis and has proven capable of detecting signal features that correlate with concussions in patients, but only under relatively static conditions. Highly unreliable signals appear when the electrodes have poor contact with wearers' skin during constant or extreme body movements. The noise caused by less-than-ideal conditions profoundly limited the applicability of this technique in real-world use cases [64]. On the other hand, MEMS accelerometers and gyroscopes coped relatively well under rough testing conditions and were applied in numerous head impact sensing approaches in laboratory and commercial settings with different mounting locations such as headgear, teeth, skin, ear canal, etc. [65-67]. However, dislocations of the accelerometers and gyroscopes from their points of attachments to body parts may result in under- or over-estimation of the acceleration signals, which limit the head injury prediction accuracies. Fiber-optic sensors have become popular in wearable detection or sensing devices, and differ from conventional approaches in their small size, low mass, and multi-sensing capabilities. This study successfully demonstrated the feasibility of using a single FBG sensor-embedded smart helmet prototype for *in situ* detection of concussive events.

The measurement system presented herein has demonstrated the ability to distinguish between different types of impactors used to induce blunt-force impact events, as shown by the data in Figure 5. Clear peak and valley patterns were shown within the first 80 – 100 ms of the transient oscillatory signals, which are unique to the tools (Allen wrench, hammer, and simulated pugil stick) that were used to strike the helmet. Thus, the signal patterns can serve as specific “fingerprints” to identify these implements and can be further trained in ML for future automatic prediction. In some cases, the signals caused by blunt-force impacts were observed to repeat over time. For example, the Allen wrench impact signal was observed repeating at a lower amplitude after approximately 10 ms. When the pugil stick was used to strike the helmet, multiple repeats of the impact signals appeared. These repeating signals may be due to shockwaves that bounced back in the internal structures of the helmet, or due to the excitation of the resonance of the rigid helmet shell. Butz et al. noted similar effects and emphasized that signal resonance could interfere with the collection of useful data [56]. In order to eliminate noise, their fixed-fixed beam was specifically designed such that the FBG sensor was immobilized to avoid background resonance during impact-induced beam deformation [56]. Despite the appearance of repeating signals in this study, the unique blunt force impact transients detected by the FBG sensor embedded in a prototype smart helmet suggest that it is possible to identify the different types of implements that caused them. Wider examples may include sharp metal objects, cement debris, and rock materials that would be encountered from explosions on the battlefield.

It is noteworthy that Butz et al. experimented with an FBG sensor similar to the sensor employed in this study. However, while their use of a superstructure to immobilize the sensor helped them measure forces that were loaded perpendicular to the sensor beam [56, 68], it hindered their potentiality to detect multi-directional impact signals as exemplified in this study. The bare fiber sensor infrastructure's ability to detect multi-directional impact events with "fingerprint " signal features in the proposed system may be due to the specific shear strains that arise within the fiber [69]. Signal peaks and valleys that occurred within 30-40 ms of impact repeatedly appeared at the same time points, even when the PIS was used to cause impacts at different magnitudes of force. Thus, the data can be used to refine the aforementioned transient data "fingerprints" for a specific impact direction. Limited linear correlation range between the peak height (or valley depth) and the kinetic impact energy was concluded from quantitative measurements (Figure 6). This is especially reflected in the early-stage major peaks or valleys, such as the first four peaks/valleys in the 0° and 270° plots, the first three peaks/valleys in the 90° plot, and the first five peaks/valleys in the 180° plots, respectively. Early-stage signals are less likely to be influenced by the structural resonance noise caused by the residue shockwaves, and therefore may better correlate with the initial impact energy levels at higher accuracy.

A combined ML model with an unsophisticated sensor design was demonstrated to produce a sensor system with high accuracy. (Figure 7 and 8). The synthesis of these elements allowed us to avoid tedious calibration as would otherwise be expected with the use of finite element analysis (FEA), as well as the difficulties associated with the inclusion of a superstructure to support the sensor. The SVM, GPR, and RF models outperformed other standalone models, and the following reasons explain their superior performances. (1) The SVM model can make good predictions when trained with high dimensional datasets, which is the case in this study. The datasets collected from this research provided detailed information that correlates FBG signals with initial impact energies and directions, thus providing a plausible multi-dimensional data structure for the training of the SVM model. (2) The good Gaussian distribution between sensor signals and impact kinetic energy from the raw data supported the good performance of the GPR model. (3) The RF model performed well by keeping the bias and variance low via growing many unpruned trees that split the high dimensional datasets. Moreover, when combining standalone models together into ensemble models, even better performances are observed. The ensemble ML model “voting” generates the best result in Figure 7 because it combines the predictions of the RF and GPR model in a metaheuristic manner and compensates the errors made by standalone models. The ensemble model AR-RF performed the best (as shown in Figure 8) because of the “boosting” effect of the additive regression (AR) process that progressively finetunes the parameters of the RF model until the deviations between predictions and actual observations reach their global minima [57, 58]. On the contrary, the IBK model is ranked last (as shown in Figure 7) because it requires substantially more data and diversity in the database. The IBK, therefore, is not the right candidate model for predictions of impact directions.

Finally, it has been reported that the location of the impact could be a strong predictor of head injury risks [56]. The ability to localize the impact locations with corresponding temporal force distributions could substantially augment the understanding of the biomechanical mechanisms of the head injury. Conventional approaches, such as arrays of mechanical sensors, can theoretically be used to monitor a large area of interest, and thus help locate the impact positions. However, researchers may find it difficult or nearly impossible to acquire any viable data on portable equipment using this method due to the size and mass of the sensors and wiring. In the system presented herein, the combination of FBG with ML models enables wearable sensing and convenient data processing without sacrificing the helmet's inner space. It also allows the detection of impact location based on the "fingerprint" signal features. Though more work is needed to further correlate these "fingerprints" with neurological or neuropathological traits, a vision of real-time sensing and analysis for immediate identification of blunt-force impact events with high spatiotemporal resolution is on the horizon.

5. CONCLUSION

In this work, a single FBG-embedded smart helmet prototype was presented as a neurological or neuropathological tool for immediate sensing of blunt-force impact events. High rate of data processing at 5 kHz enabled real-time sensing. Different types of impactors used to simulate blunt-force impact events were found to cause distinctive signal patterns. Impact magnitudes and directions were found to uniquely correlate with distinctive “fingerprint” patterns of peaks and valleys that appeared in the raw oscillatory signals. Standalone and ensemble ML models were employed for the accurate prediction of blunt force impact events. High prediction accuracy was achieved for both the impact energy levels and directions, especially with the ensemble ML models. The combination of the FBG sensor-embedded smart helmet prototype with ML models greatly simplified the data analysis process. This advantage may provide accurate guidance for *in situ* neuropathological diagnoses of blunt-force impact events in real-time. Future work will focus on the use of multi-FBG fiber-in-line configurations to aid high temporospatial resolution sensing, as well as the dual-monitoring of both blunt force impacts and blast shockwaves.

ACKNOWLEDGEMENT

This project was supported by the Leonard Wood Institute through a Cooperative Agreement with the United States Army Research Laboratory (W911NF-07-2-0062). The authors express their gratitude for the Acute Effects of Neurotrauma Consortium in assisting and coordinating the conduct of the project at Fort Leonard Wood.

PUBLICATION LEGEND

This project was supported by the Leonard Wood Institute through a Cooperative Agreement with the United States Army Research Laboratory (W911NF-07-2-0062). The authors express their gratitude for the Acute Effects of Neurotrauma Consortium in assisting and coordinating the conduct of the project at Fort Leonard Wood.

REFERENCES

Brenner LA, Vanderploeg RD, Terrio H. Assessment and diagnosis of mild traumatic brain injury, posttraumatic stress disorder, and other polytrauma conditions: burden of adversity hypothesis. Rehabilitation Psychology, 2009; 54: 239.

Butz RC, Dennison CR. In-fiber Bragg grating impact force transducer for studying head–helmet mechanical interaction in head impact. J. Lightwave Technol., 2015; 33: 2831-8.

Butz RC, Knowles BM, Newman JA, Dennison CR. Effects of external helmet accessories on biomechanical measures of head injury risk: An ATD study using the HYBRIDIII headform. Journal of biomechanics, 2015; 48: 3816-24.

Cheriyan AM, Jarvi AO, Kalbarczyk Z, Gallagher TM, Iyer RK, Watkin KL. Pervasive embedded systems for detection of traumatic brain injury. 2009 IEEE International Conference on Multimedia and Expo. IEEE, 2009: 1704-7.

Chou J-S, Chiu C-K, Farfoura M, Al-Taharwa I. Optimizing the prediction accuracy of concrete compressive strength based on a comparison of data-mining techniques. Journal of Computing in Civil Engineering, 2011; 25: 242-53.

Chou J-S, Tsai C-F, Pham A-D, Lu Y-H. Machine learning in concrete strength simulations: Multi-nation data analytics. Construction and Building Materials, 2014; 73: 771-80.

Cook R, Lapeyre J, Ma H, Kumar A. Prediction of Compressive Strength of Concrete: Critical Comparison of Performance of a Hybrid Machine Learning Model with Standalone Models. Journal of Materials in Civil Engineering, 2019; 31: 04019255.

Dinh MM, Bein K, Roncal S, Byrne CM, Petchell J, Brennan J. Redefining the golden hour for severe head injury in an urban setting: the effect of prehospital arrival times on patient outcomes. Injury, 2013; 44: 606-10.

Dinovitzer HA, Laronche A, Albert J. Fiber Bragg Grating High Impact Force Sensors with Adjustable Sensitivity and Dynamic Dynamic Range. IEEE Sensors Journal, 2019.

Faul M, Wald MM, Xu L, Coronado VG. Traumatic brain injury in the United States; emergency department visits, hospitalizations, and deaths, 2002-2006. 2010.

Grattan K, Sun T. Fiber optic sensor technology: an overview. Sensor. Actuat. A-Phys., 2000; 82: 40-61.

Guan B-O, Tam H-Y, Tao X-M, Dong X-Y. Simultaneous strain and temperature measurement using a superstructure fiber Bragg grating. IEEE Photonic. Tech. L, 2000; 12: 675-7.

Guskiewicz KM, Marshall SW, Bailes J, McCrea M, Harding HP, Matthews A, Mihalik JR, Cantu RC. Recurrent concussion and risk of depression in retired professional football players. Medicine and science in sports and exercise, 2007; 39: 903.

Han T, Siddique A, Khayat K, Huang J, Kumar A. An ensemble machine learning approach for prediction and optimization of modulus of elasticity of recycled aggregate concrete. Construction and Building Materials, 2020a; 244: 118271.

Han T, Stone-Weiss N, Huang J, Goel A, Kumar A. Machine learning as a tool to design glasses with controlled dissolution for healthcare applications. Acta Biomaterialia, 2020b.

Harper B, Aron A, Siyufy A, Mickle A, Cox K. Feasibility Assessment of the Reebok CHECKLIGHT™ and King-Devick tests as Screening tools in Youth Football. Journal of Sports Medicine and Allied Health Sciences: Official Journal of the Ohio Athletic Trainers Association, 2018; 4: 1.

Hernandez F, Wu LC, Yip MC, Laksari K, Hoffman AR, Lopez JR, Grant GA, Kleiven S, Camarillo DB. Six degree-of-freedom measurements of human mild traumatic brain injury. Annals of biomedical engineering, 2015; 43: 1918-34.

Ho Y-T, Huang A-B, Lee J-T. Development of a fibre Bragg grating sensored ground movement monitoring system. Meas. Sci. Technol., 2006; 17: 1733.

Hoge CW, McGurk D, Thomas JL, Cox AL, Engel CC, Castro CA. Mild traumatic brain injury in US soldiers returning from Iraq. New England journal of medicine, 2008; 358: 453-63.

Jarajreh MA, Giacoumidis E, Aldaya I, Le ST, Tsokanos A, Ghassemlooy Z, Doran NJ. Artificial neural network nonlinear equalizer for coherent optical OFDM. IEEE Photonic. Tech. L, 2014; 27: 387-90.

Karanov B, Chagnon M, Thouin F, Eriksson TA, Bülow H, Lavery D, Bayvel P, Schmalen L. End-to-end deep learning of optical fiber communications. J. Lightwave Technol., 2018; 36: 4843-55.

Kimpara H, Iwamoto M. Mild Traumatic Brain Injury Predictors Based on Angular Accelerations During Impacts. Annals of Biomedical Engineering, 2012; 40: 114-26.

Lee B. Review of the present status of optical fiber sensors. Opt. Fiber Technol., 2003; 9: 57-79.

Makarenko AV. Deep learning algorithms for signal recognition in long perimeter monitoring distributed fiber optic sensors. 2016 IEEE 26th International Workshop on Machine Learning for Signal Processing (MLSP). IEEE, 2016: 1-6.

Mazid AM, Ali AS. Opto-tactile sensor for surface texture pattern identification using support vector machine. 2008 10th International Conference on Control, Automation, Robotics and Vision. IEEE, 2008: 1830-5.

Muller MS, Buck TC, El-Khozondar HJ, Koch AW. Shear strain influence on fiber Bragg grating measurement systems. Journal of lightwave technology, 2009; 27: 5223-9.

Newgard CD, Meier EN, Bulger EM, Buick J, Sheehan K, Lin S, Minei JP, Barnes-Mackey RA, Brasel K, Investigators R. Revisiting the "golden hour": an evaluation of out-of-hospital time in shock and traumatic brain injury. Annals of emergency medicine, 2015; 66: 30-41. e3.

Rao Y-J. Recent progress in fiber-optic extrinsic Fabry–Perot interferometric sensors. Opt. Fiber Technol., 2006; 12: 227-37.

Tejedor J, Macias-Guarasa J, Martins H, Pastor-Graells J, Corredera P, Martin-Lopez S. Machine learning methods for pipeline surveillance systems based on distributed acoustic sensing: A review. Applied Sciences, 2017; 7: 841.

Von Rosenberg W, Chanwimalueang T, Goverdovsky V, Looney D, Sharp D, Mandic DP. Smart helmet: Wearable multichannel ECG and EEG. IEEE journal of translational engineering in health and medicine, 2016; 4.

Wang D, Zhang M, Li Z, Cui Y, Liu J, Yang Y, Wang H. Nonlinear decision boundary created by a machine learning-based classifier to mitigate nonlinear phase noise. 2015 European Conference on Optical Communication (ECOC). IEEE, 2015: 1-3.

Wu LC, Nangia V, Bui K, Hammoor B, Kurt M, Hernandez F, Kuo C, Camarillo DB. In vivo evaluation of wearable head impact sensors. Annals of biomedical engineering, 2016; 44: 1234-45.

Young BA, Hall A, Pilon L, Gupta P, Sant G. Can the compressive strength of concrete be estimated from knowledge of the mixture proportions?: New insights from statistical analysis and machine learning methods. Cement and Concrete Research, 2019; 115: 379-88

SECTION

2. CONCLUSIONS

In conclusion, the aim of this research is not only to design and develop robust FOS with promising sensing performances, but also to expand the functionality of FOS with the assist from ML. First, novel optical fiber EFPI for 1-D and 2-D tilt measurements with ultra-high resolution was demonstrated. Compared to in-line fiber optic inclinometers, an extrinsic sensing motif was used in our prototype inclinometer. With a special design, the variation in the tilt angle of the inclinometer was converted into the cavity length change of EFPI. Owing to the capabilities of EFPI sensors in high resolution displacement measurements, the proposed inclinometer can probe changes as small as 20 nanoradians. We have demonstrated that the prototype 1-D FOI can indirectly sense the inclination of a cement building (~1 micro-radian) due to the movement of clouds in the sky. The variations in tilt angle of the inclinometer was converted into the cavity length changes of the EFPI which can be accurately measured with high resolution. The developed fiber optic inclinometers showed high resolution and great temperature stability in both experiments and practical applications. Moreover, a smart helmet was developed with a single embedded FBG sensor for real-time sensing of blunt-force impact events to helmets. The FBG-embedded football helmet served as a force transducer and converted the impact events with different features into a unique transient strain variation on FBG. The combination of the transient impact data from FBG and the analyses using machine-learning model provides accurate predictions of the magnitudes, the directions and the types of the impact events. The use of the developed smart helmet system can serve as an early-stage intervention strategy for mitigating and managing traumatic brain injuries within the Golden Hour.

It is forseeable that the completion of this research combinating ML with high performance FOS will inspire the researchers in the field of sensing with a new perspective in fiber optic sensing system design and boost the progress of developing new generation of FOS for sophisticated sensing application in industry and military area.

BIBLIOGRAPHY

[1] A. Kelly, *Test Methods, Nondestructive Evaluation and Smart Materials*. Elsevier, 2000.

[2] J. F. Ready, *Industrial applications of lasers*. Elsevier, 1997.

[3] H.-N. Li, D.-S. Li, and G.-B. Song, "Recent applications of fiber optic sensors to health monitoring in civil engineering," *Engineering structures,* vol. 26, no. 11, pp. 1647-1657, 2004.

[4] L. Deng and C. Cai, "Applications of fiber optic sensors in civil engineering," *Structural Engineering and Mechanics,* vol. 25, no. 5, pp. 577-596, 2007.

[5] D.-H. Kim and M. Q. Feng, "Real-time structural health monitoring using a novel fiber-optic accelerometer system," *IEEE Sensors Journal,* vol. 7, no. 4, pp. 536-543, 2007.

[6] J. M. López-Higuera, L. R. Cobo, A. Q. Incera, and A. Cobo, "Fiber optic sensors in structural health monitoring," *Journal of lightwave technology,* vol. 29, no. 4, pp. 587-608, 2011.

[7] R. Tennyson, A. Mufti, S. Rizkalla, G. Tadros, and B. Benmokrane, "Structural health monitoring of innovative bridges in Canada with fiber optic sensors," *Smart materials and Structures,* vol. 10, no. 3, p. 560, 2001.

[8] G. C. Kahandawa, J. Epaarachchi, H. Wang, and K. Lau, "Use of FBG sensors for SHM in aerospace structures," *Photonic Sensors,* vol. 2, no. 3, pp. 203-214, 2012.

[9] V. Latini, V. Striano, G. Coppola, and I. Rendina, "Fiber optic sensors system for high-temperature monitoring of aerospace structures," in *Photonic Materials, Devices, and Applications II*, 2007, vol. 6593: International Society for Optics and Photonics, p. 65930S.

[10] S. Minakuchi and N. Takeda, "Recent advancement in optical fiber sensing for aerospace composite structures," *Photonic Sensors,* vol. 3, no. 4, pp. 345-354, 2013.

[11] N. Mrad and G. Z. Xiao, "Multiplexed fiber Bragg gratings for potential aerospace applications," in *2005 International Conference on MEMS, NANO and Smart Systems*, 2005: IEEE, pp. 359-363.

[12] H. Guo, G. Xiao, N. Mrad, and J. Yao, "Fiber optic sensors for structural health monitoring of air platforms," *Sensors,* vol. 11, no. 4, pp. 3687-3705, 2011.

[13] A. Dandridge and G. B. Cogdell, "Fiber optic sensors for navy applications," *IEEE LCS,* vol. 2, no. 1, pp. 81-89, 1991.

[14] G. A. Sanders *et al.*, "Fiber optic gyro development at Honeywell," in *Fiber Optic Sensors and Applications XIII*, 2016, vol. 9852: International Society for Optics and Photonics, p. 985207.

[15] M. Roman *et al.*, "A spatially distributed fiber-optic temperature sensor for applications in the steel industry," *Sensors,* vol. 20, no. 14, p. 3900, 2020.

[16] K. Bohnert, H. Brandle, M. G. Brunzel, P. Gabus, and P. Guggenbach, "Highly accurate fiber-optic DC current sensor for the electrowinning industry," *IEEE Transactions on industry applications,* vol. 43, no. 1, pp. 180-187, 2007.

[17] S.-I. Ohira *et al.*, "A fiber optic sensor with a metal organic framework as a sensing material for trace levels of water in industrial gases," *Analytica chimica acta,* vol. 886, pp. 188-193, 2015.

[18] Y. Fan and M. Kahrizi, "Characterization of a FBG strain gage array embedded in composite structure," *Sensors and Actuators A: Physical,* vol. 121, no. 2, pp. 297-305, 2005.

[19] N. Kuse, A. Ozawa, and Y. Kobayashi, "Static FBG strain sensor with high resolution and large dynamic range by dual-comb spectroscopy," *Optics express,* vol. 21, no. 9, pp. 11141-11149, 2013.

[20] R. Li, Y. Chen, Y. Tan, Z. Zhou, T. Li, and J. Mao, "Sensitivity enhancement of FBG-based strain sensor," *Sensors,* vol. 18, no. 5, p. 1607, 2018.

[21] W. Li, C. Xu, S. C. M. Ho, B. Wang, and G. Song, "Monitoring concrete deterioration due to reinforcement corrosion by integrating acoustic emission and FBG strain measurements," *Sensors,* vol. 17, no. 3, p. 657, 2017.

[22] J. Jung, H. Nam, B. Lee, J. O. Byun, and N. S. Kim, "Fiber Bragg grating temperature sensor with controllable sensitivity," *Applied optics,* vol. 38, no. 13, pp. 2752-2754, 1999.

[23] Y.-J. Rao, D. J. Webb, D. A. Jackson, L. Zhang, and I. Bennion, "In-fiber Bragg-grating temperature sensor system for medical applications," *Journal of Lightwave Technology,* vol. 15, no. 5, pp. 779-785, 1997.

[24] B. Zhang and M. Kahrizi, "High-temperature resistance fiber Bragg grating temperature sensor fabrication," *IEEE sensors journal,* vol. 7, no. 4, pp. 586-591, 2007.

[25] T. Li *et al.*, "Study on the non-contact FBG vibration sensor and its application," *Photonic Sensors,* vol. 5, no. 2, pp. 128-136, 2015.

[26] Y. Weng *et al.*, "A robust and compact fiber Bragg grating vibration sensor for seismic measurement," *IEEE sensors journal,* vol. 12, no. 4, pp. 800-804, 2011.

[27] F. Zhang *et al.*, "Internal combustion engine fault identification based on FBG vibration sensor and support vector machines algorithm," *Mathematical Problems in Engineering,* vol. 2019, 2019.

[28] Y. Zhuang *et al.*, "Fiber optic sensor embedded smart helmet for real-time impact sensing and analysis through machine learning," *Journal of neuroscience methods,* vol. 351, p. 109073, 2021.

[29] V. Ahsani, F. Ahmed, M. B. Jun, and C. Bradley, "Tapered fiber-optic mach-zehnder interferometer for ultra-high sensitivity measurement of refractive index," *Sensors,* vol. 19, no. 7, p. 1652, 2019.

[30] P. Chen, X. Shu, and K. Sugden, "Ultra-compact all-in-fiber-core Mach–Zehnder interferometer," *Optics letters,* vol. 42, no. 20, pp. 4059-4062, 2017.

[31] X. Li, L. V. Nguyen, Y. Zhao, H. Ebendorff-Heidepriem, and S. C. Warren-Smith, "High-sensitivity Sagnac-interferometer biosensor based on exposed core microstructured optical fiber," *Sensors and Actuators B: Chemical,* vol. 269, pp. 103-109, 2018.

[32] B. Wu, C. Zhao, B. Xu, and Y. Li, "Optical fiber hydrogen sensor with single Sagnac interferometer loop based on vernier effect," *Sensors and Actuators B: Chemical,* vol. 255, pp. 3011-3016, 2018.

[33] R. Chu *et al.*, "All-optical graphene-oxide humidity sensor based on a side-polished symmetrical twin-core fiber Michelson interferometer," *Sensors and Actuators B: Chemical,* vol. 284, pp. 623-627, 2019.

[34] L. Yuan, J. Yang, Z. Liu, and J. Sun, "In-fiber integrated Michelson interferometer," *Optics letters,* vol. 31, no. 18, pp. 2692-2694, 2006.

[35] K. D. Oh, J. Ranade, V. Arya, A. Wang, and R. O. Claus, "Optical fiber Fabry-Perot interferometric sensor for magnetic field measurement," *IEEE Photonics Technology Letters,* vol. 9, no. 6, pp. 797-799, 1997.

[36] Y.-J. Rao, "Recent progress in fiber-optic extrinsic Fabry–Perot interferometric sensors," *Optical Fiber Technology,* vol. 12, no. 3, pp. 227-237, 2006.

[37] Q. Yu and X. Zhou, "Pressure sensor based on the fiber-optic extrinsic Fabry-Perot interferometer," *Photonic Sensors,* vol. 1, no. 1, pp. 72-83, 2011.

[38] J. Huang, "Optical fiber based microwave-photonic interferometric sensors," Clemson University, 2015.

[39] R. Claus, M. Gunther, A. Wang, and K. Murphy, "Extrinsic Fabry-Perot sensor for strain and crack opening displacement measurements from-200 to 900 degrees C," *Smart Materials and structures,* vol. 1, no. 3, p. 237, 1992.

[40] Y. Du, Y. Chen, Y. Zhuang, C. Zhu, F. Tang, and J. Huang, "Probing nanostrain via a mechanically designed optical fiber interferometer," *IEEE Photonics Technology Letters,* vol. 29, no. 16, pp. 1348-1351, 2017.

[41] Y. Huang, T. Wei, Z. Zhou, Y. Zhang, G. Chen, and H. Xiao, "An extrinsic Fabry–Perot interferometer-based large strain sensor with high resolution," *Measurement science and technology,* vol. 21, no. 10, p. 105308, 2010.

[42] Y. Rao *et al.*, "Simultaneous strain and temperature measurement of advanced 3-D braided composite materials using an improved EFPI/FBG system," *Optics and lasers in Engineering,* vol. 38, no. 6, pp. 557-566, 2002.

[43] C. Zhu *et al.*, "A displacement sensor with centimeter dynamic range and submicrometer resolution based on an optical interferometer," *IEEE Sensors Journal,* vol. 17, no. 17, pp. 5523-5528, 2017.

[44] C. Zhu *et al.*, "An optical interferometric triaxial displacement sensor for structural health monitoring: Characterization of sliding and debonding for a delamination process," *Sensors,* vol. 17, no. 11, p. 2696, 2017.

[45] W. Wang, D. Ding, N. Chen, F. Pang, and T. Wang, "Quasi-distributed IFPI sensing system demultiplexed with FFT-based wavelength tracking method," *IEEE Sensors Journal,* vol. 12, no. 9, pp. 2875-2880, 2012.

[46] R. Wang and X. Qiao, "Intrinsic fabry-perot interferometeric sensor based on microfiber created by chemical etching," *Sensors,* vol. 14, no. 9, pp. 16808-16815, 2014.

[47] C. Zhu, R. E. Gerald II, Y. Chen, and J. Huang, "One-dimensional sensor learns to sense three-dimensional space," *Optics Express,* vol. 28, no. 13, pp. 19374-19389, 2020.

[48] A. G. Leal-Junior, V. Campos, C. Díaz, R. M. Andrade, A. Frizera, and C. Marques, "A machine learning approach for simultaneous measurement of magnetic field position and intensity with fiber Bragg grating and magnetorheological fluid," *Optical Fiber Technology,* vol. 56, p. 102184, 2020.

[49] N. D. Nordin, M. S. D. Zan, and F. Abdullah, "Comparative Analysis on the Deployment of Machine Learning Algorithms in the Distributed Brillouin Optical Time Domain Analysis (BOTDA) Fiber Sensor," in *Photonics*, 2020, vol. 7, no. 4: Multidisciplinary Digital Publishing Institute, p. 79.

[50] Z. Peng *et al.*, "Distributed fiber sensor and machine learning data analytics for pipeline protection against extrinsic intrusions and intrinsic corrosions," *Optics Express,* vol. 28, no. 19, pp. 27277-27292, 2020.

[51] B. Wang *et al.*, "Towards Detecting Red Palm Weevil Using Machine Learning and Fiber Optic Distributed Acoustic Sensing," *Sensors,* vol. 21, no. 5, p. 1592, 2021.

[52] Y. Zhuang, Y. Chen, C. Zhu, R. E. Gerald, and J. Huang, "Probing changes in tilt angle with 20 nanoradian resolution using an extrinsic Fabry-Perot interferometer-based optical fiber inclinometer," *Optics express,* vol. 26, no. 3, pp. 2546-2556, 2018.

[53] Y. Zhuang, Y. Chen, C. Zhu, R. E. Gerald, Y. Tang, and J. Huang, "A High-Resolution 2-D Fiber Optic Inclinometer for Structural Health Monitoring Applications," *IEEE Transactions on Instrumentation and Measurement,* vol. 69, no. 9, pp. 6544-6555, 2020.

[54] C. Zhu, Y. Chen, R. E. Gerald, and J. Huang, "Probing Changes in Pressure With Subpascal Resolution Using an Optical Fiber Fabry–Perot Interferometer," *IEEE Transactions on Instrumentation and Measurement,* vol. 69, no. 9, pp. 6556-6563, 2020.

VITA

Yiyang Zhuang was born on July 16th, 1992 in Fuan, Fujian Province, China. In June 2014, he received his Bachelor's degree in Information Engineering from Nanjing University in Nanjing, Jiangsu Province, China. In August 2015, he joined Dr. Jie Huang's Lightwave Technology Lab. He received a Master of Science in Electrical Engineering from Missouri University of Science and Technology in May 2018. And he also received his Ph.D. Degree in Electrical Engineering from Missouri University of Science and Technology in May 2021.